THESIS FOR THE DEGREE OF LICENTIATE OF ENGINEERING

Advancing Nanofluidic Scattering Microscopy for Label-Free Single-Particle Measurements

LEYLA BECKERMAN

Department of Physics and Astronomy

CHALMERS UNIVERSITY OF TECHNOLOGY

Gothenburg, Sweden 2026

Advancing Nanofluidic Scattering Microscopy for Label-Free Single-Particle Measurements
LEYLA BECKERMAN

Department of Physics and Astronomy
Chalmers University of Technology
SE-412 96 Gothenburg
Sweden
Telephone + 46 (0)31-772 1000

Cover:
The cover image shows a nanofluidic channel representative of those used in this thesis for the detection and characterization of biological nanoparticles, which in the cover image can be seen to diffuse through the channel.

Printed by Chalmers Digitaltryck
Gothenburg, Sweden 2026

"Curiouser and curiouser!"

- Alice, *Alice in Wonderland*

Abstract

Detection and characterization of biomolecules and biological nanoparticles at the single-molecule and single-particle level is important in fundamental biophysics and applied fields such as therapeutics and diagnostics. However, relying on ensemble methods for their characterization may obscure inherent heterogeneity, including subpopulations or conformations with distinct functional roles. There is also a need for analytical techniques that do not use fluorescent labels or physical tethers that might alter the physicochemical properties of the analyte. In response, label-free optical approaches for single-molecule and single-particle characterization are a growing field where direct characterization of particles in their native state is enabled.

Within the field of label-free single-particle characterization, nanofluidic scattering microscopy (NSM) is a recently developed technique that combines dark-field microscopy with a nanofluidic platform to determine both size and molecular weight of diffusing particles. Detection is enabled by interference between light scattered by the particle and the nanochannel, yielding an optical contrast enabling characterization of proteins ranging from tens to hundreds of kilodaltons in molecular weight.

While NSM has been demonstrated for the characterization of small biomolecules, extending the technique to larger and more complex nanoparticles introduces new challenges. In particular, non-specific adsorption to nanochannel walls has been a major obstacle to NSM characterization. In manuscript **I**, we overcome this obstacle by introducing a surface passivation strategy based on the formation of a polymer brush layer using the hydrophilic copolymer poly(l-lysine)-graft-poly(ethylene glycol) (PLL-g-PEG). The protocol is effective for nanochannel cross-sectional dimensions down to 50 x 50 nm^2 and reduces non-specific adsorption by several orders of magnitude. Furthermore, the passivation enables more accurate characterization of proteins and liposomes.

Building on this improvement, manuscript **II** demonstrates how NSM can be applied to characterize biologically relevant nanoparticles. Specifically, we investigate twelve different lipid nanoparticle formulations and benchmark NSM against established techniques, such as nanoparticle tracking analysis and cryo-transmission electron microscopy, showing good agreement in inferred size distributions. Beyond size distributions, the optical contrast provides a second dimension of particle characterization, offering insights into particle composition and enabling comparison of formulations, as well as assessment of inter-sample heterogeneity.

List of Appended Papers

This thesis is based on the following appended papers:

Paper I: Leyla Beckerman, Elin Persson, Razia Batool, Joachim Fritzsche, Fredrik Westerlund, Maria Solér, Bohdan Yeroshenko and Christoph Langhammer.
PLL-PEG-based Surface Passivation for Nanofluidic Scattering Microscopy of Single Biomolecules and Biological Nanoparticles
In manuscript

Paper II: Leyla Beckerman, Sofoklis Tsompanoglou, Björn Agnarsson, Joachim Fritzsche, Samir El-Andaloussi, Bohdan Yeroshenko, Fredrik Höök and Christoph Langhammer.
Label-Free Characterization of Single mRNA-Loaded Lipid Nanoparticles using Nanofluidic Scattering Microscopy
In manuscript

My Contribution to Appended Papers

Paper I: I performed the measurements and subsequent data analysis; I made all figures; I wrote the first draft of the manuscript which was finalized together with my co-authors.

Paper II: I performed the NSM measurements together with Sofoklis Tsomanoglou; I performed the data analysis; I made all figures; I wrote the first draft of the manuscript which was finalized together with my coauthors.

Contents

1 Introduction

The history of biology is in many ways closely related to the history of microscopy, where developments in microscopy have redefined and expanded what can be observed, studied and understood[1]. One of the earliest documented examples of this is Robert Hooke's *Micrographia* from the 17th century[2]. Using a compound microscope, Hooke meticulously described the microscopic structure and organization of plants, minerals and insects. While studying cork, Hooke introduced the term "cell" to describe the porous structures that he observed. Around the same time, Antonie van Leeuwenhoek developed simple single-lens microscopes and made the first reported observations of microorganisms such as bacteria and protozoa, which he referred to as "animalcula"[1]. Together, their studies fundamentally changed our understanding of biology by revealing the previously invisible microscopic world.

A major conceptual shift in biological microscopy came later during the 20th century with the development of fluorescence microscopy, which enabled the selective visualization of specific biomolecules[1]. Central to this development was the introduction of immunofluorescence by Albert Coons in the 1940s[3], where fluorescently labeled antibodies were shown to specifically bind proteins and antigens, thereby enabling localization within cells and tissues. Later, the discovery and development of green fluorescent protein (GFP) enabled visualization of intracellular dynamics and gene expression in living systems[4]. With the development of fluorescence microscopy, biological observations were able to take the step from imaging structures toward the detection and characterization of individual

biomolecules and particles. Methods such as fluorescence single-particle tracking, enabled studies of biomolecular transport, diffusion and dynamic molecular behavior[5,6], while localization-based fluorescence methods and super-resolution microscopy further extended optical imaging below the diffraction limit[6–8].

Despite their impact on how we see and understand biology, fluorescence-based approaches have some important limitations. First, fluorescent labels may perturb the properties of the system being studied, altering processes such as protein folding, intermolecular interactions or aggregation[9–12]. Second, fluorescence measurements are inherently limited by photobleaching due to photochemical degradation and are known to "blink", where the fluorophore temporarily enters a dark state, both of which will complicate long-term observations[13]. Finally, on a more fundamental level, fluorescence-based techniques generally require prior selection and labeling the studied targets, thereby limiting the observations to predefined molecular species within otherwise complex biological environments.

The limitations of fluorescence-based methods have motivated interest in microscopy techniques that do not rely on any external labels, so-called label-free techniques. Rather than fluorescence emission, these approaches exploit the intrinsic optical properties of biological matter, such as refractive index, absorption and elastic scattering, to provide the imaging contrast[14,15]. An early example is phase contrast microscopy developed by Fritz Zernike in the 1930s, which enhanced the visibility of otherwise transparent material by utilizing the phase shifts of transmitted light and converting them into intensity differences, which could reveal subcellular structures[1,16]. More recently, the use of interferometric scattering microscopy (iSCAT) has

demonstrated that individual unlabeled nanoparticles and proteins can be detected optically through elastic scattering alone, by enhancement of their weak signal through interference with a stronger reference field[17,18].

It is within the developments toward label-free single-particle characterization that Nanofluidic Scattering Microscopy (NSM), the central technique of this thesis, is situated. NSM is a label-free optical technique capable of quantitatively characterizing single biomolecules in terms of both size and molecular weight[19,20]. By confining biomolecules within nanofluidic channels embedded in silicon dioxide, their diffusion can be monitored over an extended period of time, while the channels simultaneously enhance the molecule's optical detectability. Here, it is the strong scattering from the nanochannel itself that acts as a reference field that interferes with the weak scattering from the biomolecule, providing the detectable optical contrast. By tracking the single biomolecule as it diffuses through the nanochannel, its diffusion coefficient can be determined and, thus, its hydrodynamic size. Furthermore, the optical contrast of the biomolecule, here called the integrated optical contrast (*iOC*), is related to the optical properties of the molecule and can be, for proteins, translated into a molecular weight. In the initial work introducing the method, NSM demonstrated label-free characterization of biomolecules down to 66 kDa[20]. Later work further extended the detection limit into the sub-10 kDa regime by combining the platform with machine learning approaches, as demonstrated on insulin[19].

Beyond small biomolecules such as proteins, there is also an interest in the characterization of larger and more complex biologically relevant nanoscale assemblies, such as extracellular vesicles (EVs) and lipid nanoparticles (LNPs). These particles typically exist in the size range of tens to hundreds

of nanometers and are more complex in their composition than proteins, as they consist of different constituents such lipids, proteins and nucleic acids[21,22]. Interest in these systems is of both fundamental and practical nature. EVs are secreted by cells and play important roles in cell-to-cell communication, while also possessing diagnostic potential as disease biomarkers[23]. LNPs are synthetically formulated drug-delivery vehicles currently used in mRNA-based vaccines and increasingly explored for broader therapeutic applications[24–26].

Importantly, EVs and LNPs have substantial inherent heterogeneity. Cells release multiple subpopulations of EVs, with differing molecular compositions, biological origins and physiological functions[22]. Similarly, LNP formulations show variations in size, morphology and cargo loading, where some particles may contain the encapsulated therapeutic drug, while others are empty[27–30]. It is fundamentally important to characterize the heterogeneity of these systems. In the case of EVs, understanding particle-to-particle variability is necessary to elucidate their biological functions and roles in intercellular communication and disease progression[23,31]. For LNPs, accurate characterization is critical because particle composition, morphology and payload directly influence delivery efficiency and therapeutic performance[28,32–34]. While studying EVs and LNPs, ensemble-based characterization techniques will provide an *average* over the sample population, and thus obscure rare subpopulations and biologically relevant heterogeneity. Single-particle characterization is therefore needed to resolve the underlying heterogeneity of these systems.

In the past years, different label-free single-particle techniques have been used for the characterization of heterogeneous nanoscale systems.

Interferometric nanoparticle tracking (iNTA) combines the iSCAT platform with single nanoparticle tracking (NTA) to measure size and optical signatures of biological nanoparticles[35]. This technique was demonstrated on EVs, where the optical signatures could be translated into an effective refractive index. Other integrated platforms such as single particle automated Raman trapping analysis (SPARTA)[36] and electrohydrodynamic tweezers[37] have demonstrated chemical probing of liposome and EV systems. Electrohydrodynamic tweezers have additionally enabled the simultaneous measurement of particle size on these systems, while SPARTA has demonstrated proof-of-concept sizing measurements using polystyrene particles. However, these approaches have mainly been demonstrated in the larger (> 50 nm) nanoparticle regime. NSM may be a complementary approach in this context as the platform was originally developed for characterization of significantly smaller particles. The nanofluidic environment of NSM also provides an additional degree of control over the observation conditions.

The broader aim of my research is to develop NSM toward a reliable platform for the characterization of heterogeneous biological nanoparticle systems. This thesis presents the initial steps toward this goal by addressing current methodological limitations and exploring the current capabilities of NSM for biological nanoparticle characterization. One methodological challenge in applying NSM to these systems is the mitigation of non-specific adsorption of the particles to the nanochannel walls. In **Manuscript I**, this challenge is addressed by the development of a surface passivation strategy for the nanofluidic channels. Building on this improvement, **Manuscript II** explores NSM as a tool for characterization of LNPs, demonstrating its potential as a characterization platform by combining information on both

size and optical contrast. To support the studies presented in this thesis, the following chapters will provide the necessary theoretical and experimental framework of NSM, together with descriptions of the systems studied.

2 Nanofluidic Scattering Microscopy: Theory and Implementation

As introduced in Chapter 1, Nanofluidic Scattering Microscopy (NSM) enables the label-free, real-time detection and characterization of single biomolecules in solution by a combination of nanofluidic confinement and interferometric detection[20]. At a first level of abstraction, NSM can be understood through three interconnected components, summarized in **Figure 2.1**.

i) **The nanofluidic device**, which controls the measurement environment, introducing and confining the particles within nanofluidic structures and enabling time-resolved optical detection of diffusing particles.

ii) **The optical detection principle and platform**, where light scattered from the nanochannel and particle is collected in a dark-field microscope to give the interferometric image signal.

iii) **The signal analysis framework**, where the recorded image is processed to extract the particle optical signature and quantify the two NSM experimental observables: particle diffusivity (D) and the integrated optical contrast (iOC).

The purpose of this chapter is to introduce the physical principles and experimental implementation of each of these components. First, the nanofluidic device is described, together with its functional role and a brief overview of its fabrication. Second, the interferometric detection principle is motivated and described together with the experimental microscope platform used for signal acquisition. Finally, the image processing and analysis framework used to retrieve and interpret the NSM observables are presented.

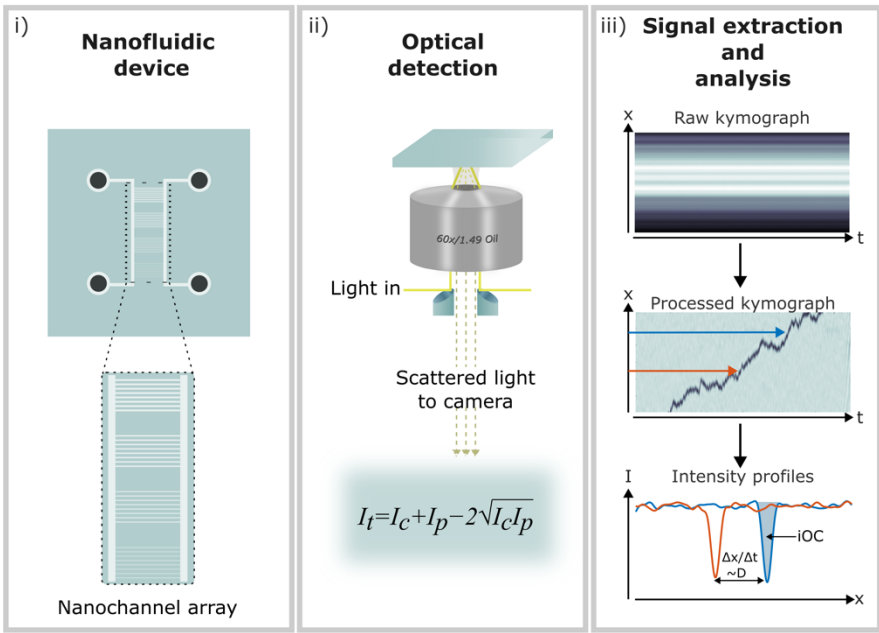

Figure 2.1 Components of NSM experiments. i) *The nanofluidic chip on which the experiments are performed.* **ii)** *Optical detection framework and dark-field microscope configuration on which the interferometric scattering signal is recorded.* **iii)** *Signal extraction and data analysis where information on particle characteristics is retrieved.*

2.1 Nanofluidic Device

Nanofluidic channels form a central component of NSM, enabling both the controlled transport and optical detection of the single particles in solution, as well as ensuring that they stay in the focal plane of the microscope for extended periods of time. The general structure of the nanofluidic device used in this thesis is shown in **Figure 2.2a**. At the largest scale, the 1 x 1 cm^2 device consists of two parallel microfluidic channels, each interfaced with

two inlet and outlet reservoirs. It is over these reservoirs that the sample is introduced and transported via the microchannels to the central nanochannel array by pressure-induced convective flow.

A magnified view of the nanochannel array is shown in **Figure 2.2b**. These nanochannels constitute the optical sensing region of the device where imaging is performed. On a single chip, there is typically a range of nanochannels with distinct cross-sectional dimensions, as the detection of smaller biomolecules require smaller channels, whereas larger structures are required to accommodate larger nanoparticles. In this thesis, nanochannels with nominal cross-sectional dimensions ranging from 50 x 50 nm^2 to 300 x 350 nm^2 were used. Representative cross-sectional SEM images of some of these are shown in **Figure 2.2d**. The SEM images show that the cross-section geometry of our nanochannels is approximately rectangular. This is why two dimensions are specified, width and depth respectively, when describing the cross-sectional area. Furthermore, and very importantly, since translation of the experimental observables *D* and *iOC* into particle size and mass both depend on the true absolute dimensions of the nanochannel, it is critical to know the exact cross-sectional area. The cross-sectional area can be extracted from the cross-sectional SEM images by manually tracing a polygon around the channel perimeter.

During an experiment, only a single nanofluidic structure is imaged, as particles traverse the nanochannel from one microchannel to the other, either by diffusion or by the application of a low convective flow (**Figure 2.2c**). Importantly, the use of nanofluidic structures in NSM measurements serve two main purposes. First, they confine the particles within the focal volume of the objective, which enables them to be detected and tracked for several

frames. Second, the light scattering from the nanochannel itself is what provides the background field required for the interferometric detection of the particles.

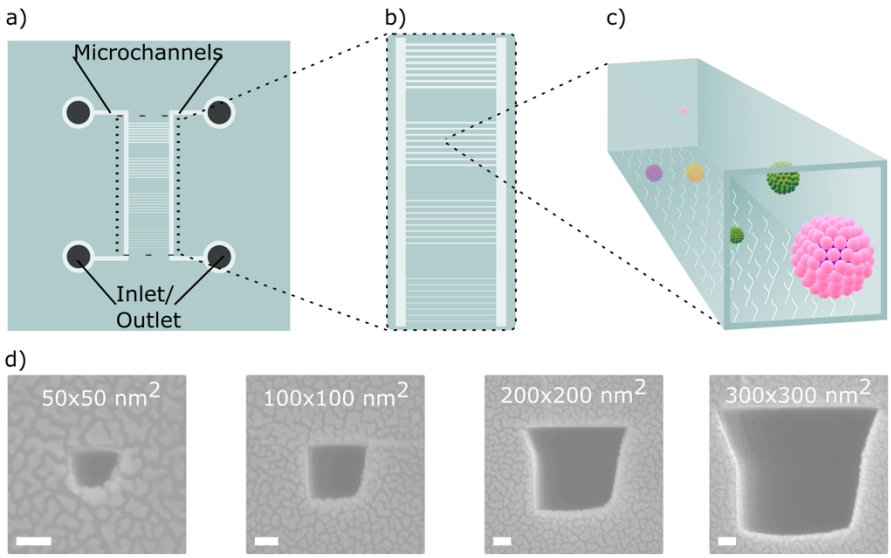

Figure 2.2 Nanofluidic chip layout and cross-sectional SEM images. a) *Layout of the nanofluidic device. Sample is introduced over the inlets and transported through the microchannels to the central nanochannel array via convective flow or diffusion.* **b)** *Central nanochannel array consisting of nanofluidic channels of various cross-sectional dimensions.* **c)** *NSM experiments are performed in a single imaged nanochannel where particles are imaged and detected as they move along the nanochannel length.* **d)** *Cross-sectional SEM images of some of the nanochannels used in this thesis. Scale bars are 50 nm.*

The micro- and nanofluidic systems are fabricated into a thermally grown silicon dioxide (SiO_2) film on a silicon wafer by reactive ion etching. The access inlet holes are etched through the backside of the silicon substrate, and the device is sealed by thermal bonding to a borosilicate glass wafer,

enabling optical imaging. A more detailed description of the fabrication procedure can be found elsewhere[19,20].

During measurements, the chip is mounted in a custom-made chip holder (**Figure 2.3**) and subsequently mounted on the microscope. The sample is introduced to the chip via the Teflon reservoirs interfacing with the inlets. To control sample flow and direction through the chip, one or more of the inlets are pressurized with N_2, inducing a convective flow in the desired direction.

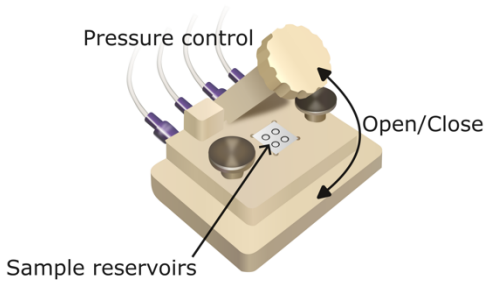

Figure 2.3 Chip holder used for sample introduction and fluidic control. *Sample is introduced at the Teflon insert reservoirs and the system is closed. Fluidic control of the sample through the nanofluidic device is exerted by pressurizing one or more of the inlets to induce convective flow through the chip in the desired direction.*

Although the nanofluidic structures are essential to the very working principle of NSM, their confined geometry might also introduce steric barriers for the particles to enter the nanochannels. This effect was observed in **Manuscript II** where characterization of a mixed polystyrene sample containing different sizes at equal ratios resulted in an apparent enrichment of the smaller particle subpopulations relative to the larger particles. Such effects are important to consider when interpreting NSM measurements, as they may distort the measured particle size distribution.

As the particle size increases relative to the nanochannel dimensions, the accessible area available for particle entry reduces because its center cannot approach the wall more closely than its radius. This reduces the probability of successful entry. Such steric exclusion effects are well known in pore filtration theory[38,39] and the partition coefficient, φ, at the entrance of a rectangular channel can be approximated by,

$$\varphi \approx \left(1 - \frac{2r_p}{h}\right)\left(1 - \frac{2r_p}{w}\right), \tag{2.1}$$

where r_p is the particle radius, h is the channel height and w is the channel width. However, the magnitude of this filtration effect may potentially be reduced through optimized nanochannel design. For example, funnel-shaped inlets could facilitate particle entry by lowering the steric barrier at the channel interface.

2.2 Optical Detection

Due to the small size, the intensity of the light scattered from nanoscale objects is typically too small for conventional optical detection. Instead, NSM uses an interferometric approach where the weak scattering of a particle or molecule confined inside a nanochannel interferes with a stronger reference field scattered by the nanochannel itself, effectively amplifying the particle signal.

To understand this effect in more detail, this section will first introduce the scattering properties of small dielectric particles and discuss the limitations in their direct scattering detection. Thereafter, the interferometric detection

principle underlying NSM measurements is described, followed by a description of the optical setup used in practice for the signal acquisition the experiments included in this thesis.

2.2.1 Scattering by a small dielectric sphere

Light scattering occurs when light encounters a particle with optical properties different from its surroundings. In transparent dielectric media such as water, the oscillating electric field of the incident light induces an optical response in both the particle and the surrounding medium. If the particle responds differently to the electric field than its surroundings, the propagation of the electromagnetic wave is perturbed. As a result, part of the incident light is reradiated into new directions, giving rise to scattered light[40].

If a particle is much smaller than the wavelength of the incident light, the electric field can be approximated as uniform across the particle's volume. In this regime, the particle can be modeled as an induced electric dipole, with a dipole moment ($\boldsymbol{p}$) proportional to the electric field ($\boldsymbol{E}$) according to[40],

$$\boldsymbol{p} = \varepsilon_m \alpha \boldsymbol{E}, \tag{2.2}$$

where ε_m is the dielectric constant of the medium and α is the polarizability of the particle. In this description, it is the oscillating dipole that reradiates electromagnetic waves, giving rise to the scattered field. The polarizability determines the strength of the optical response, as it describes how easily the charges are displaced by the external field. For a dielectric sphere much smaller than the wavelength of the incident light, the polarizability is given by,

$$\alpha_p = 3V_p \frac{\varepsilon_p - \varepsilon_m}{\varepsilon_p + 2\varepsilon_m}, \tag{2.3}$$

where V_p is the particle volume and ε_p and ε_m are the dielectric constants of the particle and the surrounding host medium, respectively. Thus, the strength of the scattered field ($\boldsymbol{E_s} \propto \alpha_p \boldsymbol{E}$) depends on both the particle's size and the dielectric contrast, i.e. the difference in the particle's optical properties relative to its surroundings.

Herein lies the crux: for tiny objects, such as proteins or other molecules, the scattered field is extremely weak due to their small volume. Furthermore, since optical detectors measure intensity, which scales with the square of the electrical field amplitude $I \propto |\boldsymbol{E}|^2$, the detected scattering signal decreases rapidly with decreasing particle size. As a result, direct detection of scattering from a single biomolecule becomes challenging. This is the motivation behind interferometric techniques such as NSM, where the weak scattered field from the particle is instead detected indirectly through an interference effect with a much stronger reference field, which in NSM is provided by the nanofluidic structure.

2.2.2 Interferometric detection

Optical interference occurs when coherent electromagnetic waves overlap, giving rise to a total electric field equal to the superposition of the individual fields. In the context of interferometric detection, where a reference field $\boldsymbol{E_{ref}}$ is used, its interference with the scattered field from the particle $\boldsymbol{E_p}$, yields a total field that can be expressed as

$$\boldsymbol{E_t} = \boldsymbol{E_{ref}} + \boldsymbol{E_p}. \tag{2.4}$$

The detected intensity is therefore[41]

$$I_t = I_{ref} + I_s + 2\left|\boldsymbol{E_{ref}}\right|\left|\boldsymbol{E_p}\right|\cos\phi, \tag{2.5}$$

where the first term corresponds to the intensity of the reference field, while the second term corresponds to the scattered intensity from the particle alone. The third term represents the interference between the two fields, where ϕ is their relative phase. Importantly, the interference term scales linearly with the scattered field amplitude which in turn is amplified by the strength of the reference field. Consequently, even extremely weak scattered fields can become detectable when combined with a sufficiently strong reference field.

The reference field differs between different interferometric imaging approaches. In, for example iSCAT[20], the reference field may either be the transmitted illumination beam through the sample, or its reflection at the sample interface[41]. In plasmonic scattering microscopy, the interference between the incident planar plasmonic wave and particle scattered plasmonic wave is instead leveraged[42]. In NSM, the reference field is provided by the scattering from the nanofluidic structure itself. Hence, the interference expression for NSM can be written as[20],

$$I_t = I_c + I_p - 2\sqrt{I_c I_p}, \tag{2.6}$$

Where I_c and I_p refer to the scattered light intensities from the channel and particle, respectively. The sign of the interference term depends on the relative phase between the two scattered fields, which within the electrostatic

approximation is determined by the sign of their polarizabilities. This in turn depends on the dielectric constants (Eq. 2.3). The nanofluidic structure can be regarded as a water-filled channel embedded in a SiO_2 matrix, giving rise to a negative polarizability ($\varepsilon_{H_2O} < \varepsilon_{SiO_2}$). The particle, which is embedded in water, conversely has a positive polarization contrast ($\varepsilon_p > \varepsilon_{H_2O}$). Hence, the scattered fields from the channel and the biomolecule are π out of phase, leading to destructive interference and a negative contrast signal.

2.2.3 Optical setup

In practice, NSM measurements are performed using a custom-built dark-field microscope. In dark-field microscopy, the illumination and scattered light are spatially separated such that only the scattered light reaches the detector, causing scattering objects to appear bright against a dark background[43]. To generate these dark-field conditions, the configuration in **Figure 2.4** is used. The incident illumination is focused onto the back-focal plane of a high numerical aperture (NA), oil-immersion objective and directed towards the nanofluidic chip under angle using a micromirror positioned at the objective back aperture. The reflected illumination beam is then removed from the optical path using a second micromirror, while the scattered light is transmitted towards the detector.

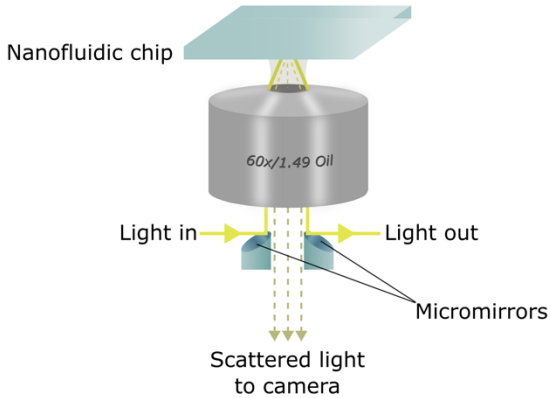

Figure 2.4 NSM dark-field microscope configuration. *Illumination of the nanofluidic chip is introduced under angle and the reflected beam is removed using two micromirrors positioned at the objective back aperature. The scattered light is collected by a high-NA oil-immersion objective and transmitted to the detector.*

A schematic overview of the full optical layout is shown in **Figure 2.5**. Broadband illumination is provided by a supercontinuum laser source (NKT), spectrally filtered to wavelengths between 500-800 nm and directed toward the sample stage. Inserted into the optical path are two flip mirrors (M1 and M2) which allow for optional rerouting of the beam through an additional expansion arm (as depicted in **Figure 2.5**). This expansion stage is primarily used for measurements in larger nanochannels, where the stronger scattering intensity allows for the illumination to be spread out over a larger field of view, enabling the imaging of approximately 60 μm of channel length. For smaller nanochannels, used for example in protein measurements, the expansion stage is instead bypassed to maintain higher illumination intensity, giving an effective field of view covering approximately 18 μm of channel length.

In addition to the broadband illumination used for NSM, the setup also incorporates a secondary excitation laser for fluorescence imaging. In the current setup, a 488 nm laser is used for the excitation of common fluorophores such as fluorescein (FITC). Before combining the two beams, the excitation beam is spatially filtered to improve beam quality, after which it is coupled into the same optical path as the broadband illumination. Following reflection at the sample surface, the excitation light is likewise removed from the optical path, while the scattered light and fluorescence emission are spectrally filtered by a dichroic beamsplitter and imaged onto separate camera detectors. The scattered intensity is imaged onto an sCMOS camera for high-speed imaging and low readout noise, while the fluorescence emission is imaged onto a qCMOS which enables single-photon detection.

Although NSM and fluorescence measurements are currently performed only separately, ongoing work aims to synchronize the two for simultaneous acquisition. Such combined measurements could provide valuable information when investigating heterogeneous or complex samples, for example by correlating fluorescent labeling with the optical signature measured by NSM. While the current setup only incorporates a 488 nm excitation laser, other excitation wavelengths can be incorporated into the optical setup for future multiplex fluorescence measurements.

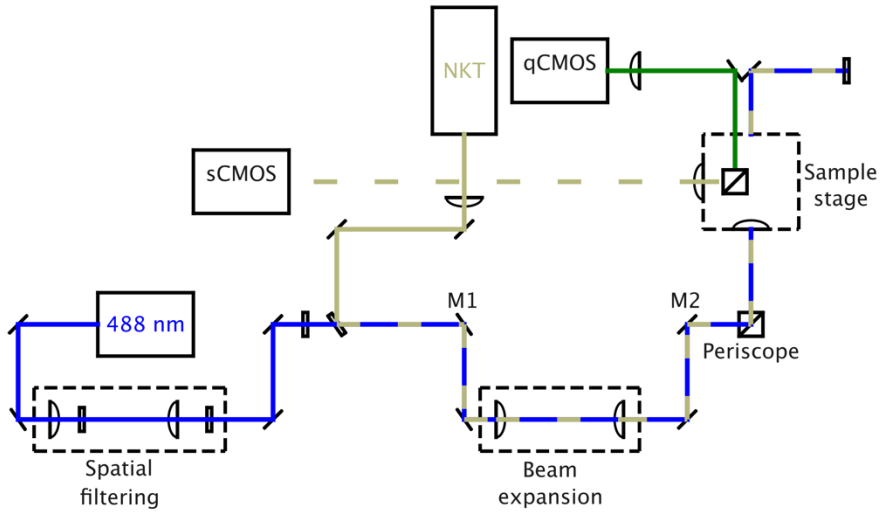

Figure 2.5 Schematic overview of the optical setup for NSM measurements. *Broadband illumination from a spectrally filtered supercontinuum laser (NKT) is directed towards the sample stage, with optional rerouting through an expansion arm via flip mirrors M1 and M2. A secondary 488 nm excitation laser can be coupled into the optical path for fluorescence measurements. Scattered light and fluorescence emission are separated spectrally and imaged onto separate camera detectors.*

2.3 Data processing and Particle Characterization

As previously described, the total intensity image recorded by the camera in an NSM experiment is comprised of three contributions according to,

$$I_t = I_c + I_p - 2\sqrt{I_c I_p},$$

where I_c is the intensity originating from the scattered light by the nanochannel, I_p is the intensity scattered by the particle and the third term is

the interferometric contribution between the two scattered fields. Since $I_c \gg I_p$, the direct particle scattering contribution can be neglected and $I_t \approx I_c - 2\sqrt{I_c I_p}$. Here, the interferometric term is the signal of interest as it contains the optical information associated with the particle or molecule to be studied. Hence, the subsequent data processing following image acquisition is centered around isolating this term and extracting the two NSM experimental observables: the integrated optical contrast, *iOC* and particle diffusivity, *D*. The workflow of this post-processing is summarized in **Figure 2.6.**

Each recorded image is first integrated along the y-axis, giving a one-dimensional intensity profile, and the images are stacked in time, yielding a raw intensity kymograph (**Figure 2.6a**). To isolate the interferometric term, differential background imaging is performed in which the static channel background intensity is subtracted from the total recorded intensity. The resulting signal is subsequently normalized by the channel background intensity, yielding an optical contrast (OC)[20]

$$OC = \frac{I_t(x) - I_c(x)}{I_c(x)} \tag{2.7}$$

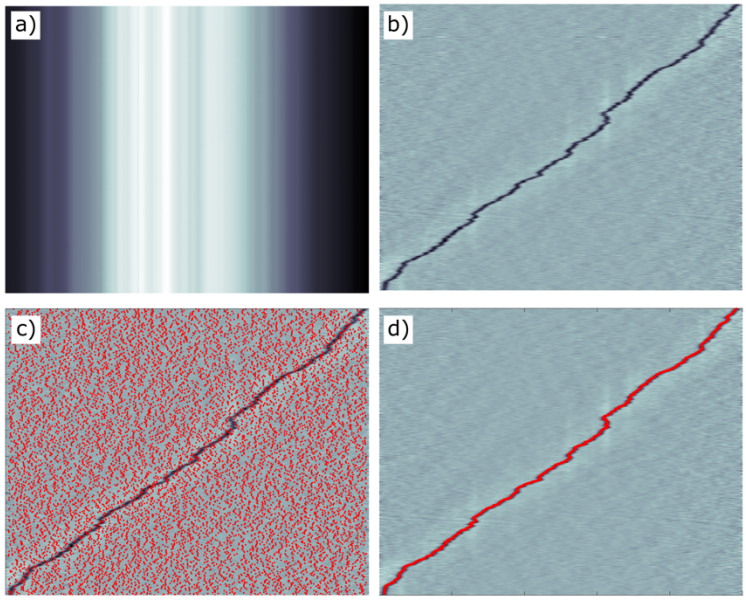

Figure 2.6 Overview of steps in NSM data post-processing. ***a)*** *Raw intensity kymograph.* ***b)*** *Processed kymograph after background subtraction.* ***c)*** *Identification of minimas.* ***d)*** *Linking of minimas into particle trajectory.*

Computationally, this is done by first estimating the background locally in both space and time using a moving median window of fixed dimensions. The processed kymograph is then obtained by subtracting the estimated background from each frame and normalizing by the channel background, yielding the processed kymograph (**Figure 2.6b**). Particle positions are then identified by detecting local minima in the optical contrast profile for each frame (**Figure 2.6c**), after which they are linked between consecutive frames based on expected particle motion between frames, where candidate trajectories with unrealistically large displacements or inconsistent optical

contrast are rejected (**Figure 2.6d**). Particle diffusivity and *iOC* are then determined from the found trajectories[20].

2.3.1 Diffusion analysis and hydrodynamic radius

The first NSM observable is the particle's diffusion coefficient, *D*, which is obtained by tracking the motion of individual particles along the nanochannel, from the position of their identified minima. If convective flow was present during the measurement, the mean drift velocity of the trajectory is first estimated and subtracted from the displacements. The diffusion constant is thereafter calculated from its mean square displacement along the channel including a correction term accounting for motion blur and localization uncertainty[20,44],

$$D = \frac{\langle \Delta x_i^2 \rangle}{2\Delta t} + \frac{\Delta x_i \Delta x_{i+1}}{\Delta \mathrm{t}}. \tag{2.8}$$

The diffusivity of a particle in bulk solution can be related to its size through the Stokes-Einstein equation,

$$HR = \frac{k_B T}{6\pi\eta D}, \tag{2.9}$$

where k_B is the Boltzmann constant, T is the temperature and η is the solution viscosity. The hydrodynamic radius, HR, represents the radius of an ideal hard sphere that diffuses at the same rate as the measured particle, and will include contributions from surface modifications and surrounding stagnant hydration layers[45].

In NSM measurements, the retrieved diffusion coefficient corresponds to an apparent diffusivity, D_{app}, which will be smaller than the diffusion coefficient in bulk. This is due to the particle motion being spatially confined in the nanochannel, and as the particle size becomes large relative to the channel dimension, hydrodynamic interactions between the particle and nanochannel walls come into effect. These will increase the viscous drag and thereby reduce the particle's diffusivity[39].

To account for this "hindered diffusion", a hindrance factor, K, is used such that the hydrodynamic radius can be inferred from the apparent diffusivity according to,

$$HR = K\frac{k_B T}{6\pi\eta D_{app}}. \tag{2.10}$$

For a freely diffusing particle in bulk, $K = 1$. K will decrease with increasing confinement. For a cylindrical pore, K is given by[39]

$$K = \frac{\left(1 + \left(\frac{9}{8}\right)\gamma \ln\gamma - 1.56\gamma + 0.53\gamma^2 + 1.92\gamma^3 - 2.82\gamma^4 + 0.27\gamma^5 + 1.10\gamma^6 - 0.44\gamma^7\right)}{(1-\gamma)^2}, \tag{2.11}$$

where $\gamma = HR/r$, and r is the radius of the pore. Due to the rectangular cross-section of the nanochannels, r is approximated as the radius of an equivalent cylindrical pore with the same cross-sectional area. To retrieve the hydrodynamic radius from measured apparent diffusivity, the confined Stokes-Einstein relation is solved iteratively, as the hindrance factor itself is a function of the hydrodynamic radius.

2.3.2 Integrated optical contrast (*iOC*) and its interpretation

The integrated optical contrast (*iOC*) is the second observable in NSM and provides a measure of the optical signal generated by the particle or molecule. For biomolecules such as proteins, the *iOC* can be converted into protein molecular weight, *MW*. For more structurally complex particles, such as lipid nanoparticles, the *iOC* instead reflects the combined optical response of size, composition and effective refractive index.

The *iOC* is obtained by integrating the optical contrast along the imaged channel length L[20],

$$iOC = \int_0^L \frac{I_t(x) - I_c(x)}{I_c(x)} dx\,, \tag{2.12}$$

providing a quantitative measure of the particle-induced interferometric contrast. Importantly, the *iOC* is directly related to the particle's polarizability, α_p, according to[20],

$$iOC = \frac{\bar{n}}{A}\alpha_p, \tag{2.13}$$

where A is the nanochannel cross-sectional area and $\bar{n} = (1.5n_{\mathrm{H_2O}}^2 + 0.5n_{\mathrm{SiO_2}}^2)/(n_{\mathrm{H_2O}}^2 - n_{\mathrm{SiO_2}}^2)$ is a prefactor determined by the refractive indices of the surrounding environment.

During post-processing, the *iOC* is determined for each frame of the particle trajectory by fitting a Gaussian function to the optical contrast profile along

the channel axis, and calculated from the fitted Gaussian amplitude, a, and width, b,[20]

$$iOC = \sqrt{\pi}ab. \tag{2.14}$$

Each trajectory is then assigned an *iOC* value taken as the median of all frames.

Translation of iOC into molecular weight

For proteins, the relationship between *iOC* and particle polarizability becomes particularly useful since the protein polarizability can, under appropriate assumptions, be related to the protein's molecular weight (*MW*).

Expressing **Eq 2.3** in terms of refractive indices ($\varepsilon_i = n_i^2$), the polarizability of a small dielectric particle is,

$$\alpha_p = 3V_p \frac{n_p^2 - n_m^2}{n_p^2 + 2n_m^2}, \tag{2.15}$$

where n_p and n_m are the refractive indices of the particle and the surrounding medium, respectively. To relate the protein polarizability to molecular weight, the particle volume is expressed using the specific volume, ($V_p = MW \cdot V_{sp}/N_A$), yielding

$$\alpha_p = \frac{3MW \cdot V_{sp}}{N_A} \frac{n_p^2 - n_m^2}{n_p^2 + 2n_m^2}, \tag{2.16}$$

where N_A is Avogadro's constant. For proteins suspended in aqueous solutions, the refractive index contrast term does not vary substantially between protein species due to the conserved composition and optical properties of amino acids[46,47]. Furthermore, protein density is close to constant and consequently, proteins have an approximately constant polarizability-to-mass ratio (α_m/MW). Using literature values for protein specific volume ($V_{sp} = 0.7446\ \mathrm{mL/g}$), protein refractive index ($n_p = 1.5867$) and refractive index of water ($n_m = 1.33$)[48], the proportionality constant can be determined as[20],

$$\frac{\alpha_p}{MW} = 0.46\ \frac{\text{Å}^3}{\text{Da}}.$$

Substituting this into **Eq. 2.13**,

$$iOC = 0.46\frac{\bar{n}}{A}MW, \tag{2.17}$$

and hence, NSM can infer a protein's molecular weight from the measured polarizability through the *iOC* under assumptions of constant protein refractive index and density. However, deviations from these assumptions occur for proteins with atypical refractive index properties due to their composition or conformation, such as proteins belonging to the crystallin family[49].

iOC for complex biological nanoparticles

The translation of *iOC* into *MW* for particles relies on two main assumptions: first, the particle must be small compared to the wavelength of light for the

dipole approximation to remain valid. Second, the proportionality between *iOC* and *MW* assumes that the particles belong to a class of materials with known and approximately constant refractive index and density. These assumptions typically hold for particles such as proteins. However, for larger and more structurally complex particles, such as lipid nanoparticles and extracellular vesicles, these assumptions are no longer valid.

As previously discussed, the underlying assumption of the dipole approximation is that the electric field is uniform over the particle volume, which is generally satisfied when the particle is much smaller than the wavelength of light. The validity of invoking the dipole approximation can be expressed as a ratio between the characteristic length and the wavelength, the so-called size parameter[50],

$$x = \frac{2\pi r_p n_m}{\lambda}, \tag{2.18}$$

where r_p is the particle radius and λ is the wavelength of the incident light. For small proteins, $x \ll 1$ and the particle can therefore be approximated as a uniformly polarized dipole. However, for particles such as lipid nanoparticles with a typical radius range of 25-100 nm, the size parameter becomes non-negligible (≈0.3-1.1). Here, the electric field can vary significantly across the particle volume, and the induced polarization is not spatially uniform resulting in higher-order electromagnetic modes contributing to the scattering response. Here, more complete descriptions of scattering, such as Mie theory for homogeneous spherical particles have to be used[40].

In the regime of Mie scattering, the angular distribution of the scattered light becomes increasingly asymmetric, where the dipolar radiation pattern characteristic of small particles become progressively dominated by forward-scattering. As a result, the fraction of the scattered light collected by the microscope becomes increasingly dependent on particle size, internal structure and optical properties of the particle, complicating the direct interpretation of the measured *iOC*. Additionally, larger channels must be used for larger particles for simple geometric reasons, and as our channels are rectangular in cross-section, Mie theory becomes limited in its applicability.

An additional complication is the structural heterogeneity of these types of particles, as they are made up of multiple components with different refractive index properties, including lipids, nucleic acids, proteins and aqueous interiors. Consequently, the concept of a single well-defined refractive index becomes less clear, and these particles are instead described using an effective refractive index, determined by the combined optical response of the material composition they are made of. Various mixing approaches, such as Maxwell-Garnett and Lorentz-Lorenz[51], can be been used to relate the effective refractive index to particle composition and internal structure.

Importantly, despite these complications, the interferometric detection principle underlying NSM remains unchanged as the measured signal still arises from interference between the scattering from the particle and the scattering from the nanochannel. However, the *iOC* measured for complex biological nanoparticles should not be interpreted directly as a molecular

weight, but instead as a reflection of the combined optical response of particle size, composition, internal structure and effective refractive index.

Despite this complexity, it is important to highlight that it is possible to still infer a value for the effective refractive index of a large complex nanoparticle, provided appropriate calibration with an optically homogeneous system of known refractive index is executed. Specifically, a set of experimental conditions needs to be controlled and remain unchanged between calibration and measurement. These conditions include the nanochannel itself, i.e. calibration and experiment must be executed in the same channel, and maintaining a consistent illumination angle and effective collection aperture. Furthermore, an appropriate set of calibration particles in the same size range with well-defined refractive indices must be used. Combining **Eq 2.13** with **Eq 2.15**, yields and expression relating the *iOC* to the effective refractive index of the particle, n_{eff}^2,

$$iOC = 3V\frac{\bar{n}}{A}\frac{n_{eff}^2 - n_m^2}{n_{eff}^2 + 2n_m^2} = 3KVN, \qquad (2.19)$$

where *K* incorporates the constant terms and *N* is the refractive index expression. By calibrating through a sample of known refractive index, *K* can be determined and used to estimate the effective refractive index of the unknown particle. Here, the estimation of the effective refractive index is illustrated on the example of liposomes (**Figure 2.7**). The NSM measurement of the liposomes revealed a population between 40 and 125 nm in diameter (**Figure 2.7a**), with a corresponding variation in *iOC*. Calibrating against polystyrene samples of nominal dimensions of 30, 50 and 70 nm in diameter with a refractive index of 1.59 measured at the same time in a nanochannel

of the same nominal dimensions, the *iOC* signal of each detected particle could be translated into an effective refractive index (**Figure 2.7b**), yielding a narrow distribution with a median n_{eff} of 1.39, in good agreement with what is expected for liposomes from literature[52].

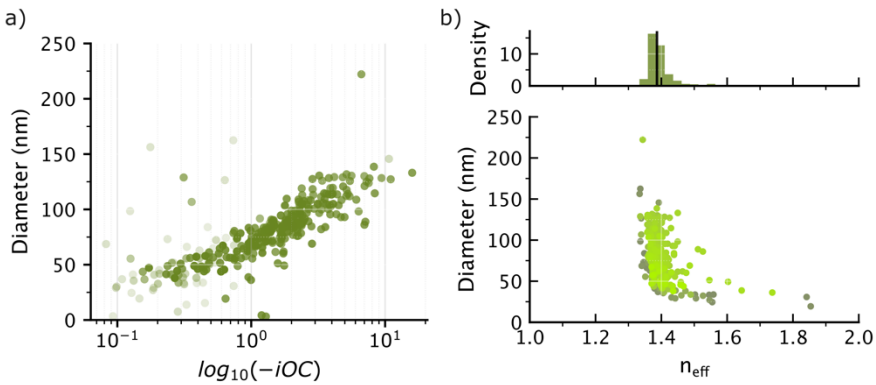

Figure 2.7 Translation of *iOC* into an effective refractive index for liposomes. *a) NSM measurement of liposomes shown as a scatter plot of diameter vs iOC (log-scale). Each point corresponds to an individual trajectory with its transparency indicating trajectory length. b) Translation of the measured iOC into an effective refractive index after calibration against polystyrene samples in nanochannels of same dimensions.*

3 The Challenge of Nonspecific Adsorption

A persistent challenge in handling biomolecules and biological nanoparticles is their tendency to nonspecifically bind and adsorb to surrounding solid-liquid interfaces. Here, "non-specific" refers to unintended interactions between the analyte and the system, in contrast to the selective binding events that many biosensing applications rely on for detection[53]. These effects are particularly critical in NSM, where particles are detected and characterized as they freely diffuse through the imaged nanochannel. In this context, non-specific interactions and adsorption can significantly complicate both detection and subsequent analysis. Transient interactions with the surface can hinder particle motion, leading to a reduction in the apparent diffusion coefficient and, consequently, an overestimation of hydrodynamic radius (**Eq 2.10**). In contrast, irreversible adsorption results in a complete loss of signal due to the differential imaging scheme applied, where static features are removed by frame subtraction.

These two scenarios are highlighted in **Figure 3.1a**, showing a processed kymograph of an apoferritin protein trajectory. Initially, transient surface interactions (1) cause the particle to temporarily halt its diffusion. Subsequently, it irreversibly adsorbs to the channel surface and disappears from the subsequent frames (2). Over time, such adsorption events lead to fouling of the nanochannel walls, resulting in practical issues including clogging, reduced throughput and ultimately loss of device functionality. An example of such nanochannel fouling is shown in the dark-field micrograph in **Figure 3.1b**.

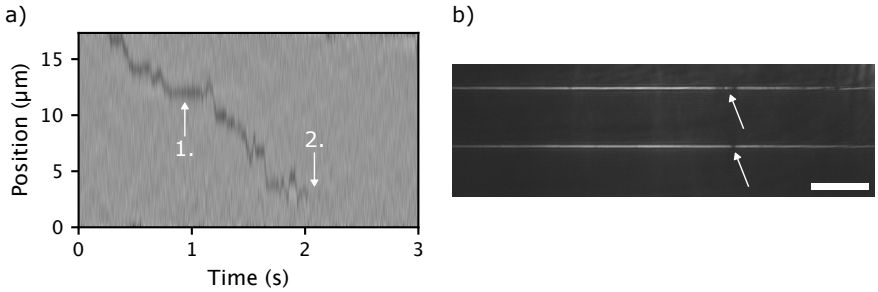

Figure 3.1 Consequences of nonspecific adsorption in NSM experiments. a) *Processed NSM kymograph showing a protein trajectory (apoferritin). Arrows point towards to two types nonspecific interactions: (1) transient binding of the protein to the channel wall and (2) complete adsorption of the protein to the channel wall where the particle trace "disappears" due to the differential imaging scheme applied.* **b)** *Dark-field image of two parallel nanochannels. Arrows point towards regions where fouling of the nanochannel has occurred an manifests itself as the channel appearing darker. Scale bar is 10 µm.*

Addressing nonspecific adsorption is essential for advancing NSM as a general method for nanoparticle characterization, particularly for systems that have strong interactions with silica surfaces[20]. In **Manuscript I**, we address this challenge by implementing a passivation strategy based on poly(L-lysine)-g-poly(ethylene glycol) (PLL-g-PEG) layers. The purpose of this chapter is to place this approach into context, by first outlining the multitude of intermolecular interactions that drive nonspecific adsorption at solid-liquid interfaces, and then discussing how these effects are amplified under nanoconfinement. Subsequently, common strategies for mitigating nonspecific adsorption are briefly reviewed, with emphasis on their applicability to nanofluidic systems. Finally, the main results of **Manuscript I** are presented together with an outlook on how the implemented surface

functionalization can be further explored in its potential use for spatially resolved bioanalytical assays.

3.1 Origins of Adsorption at Solid-Liquid Interfaces

Despite decades of study on the phenomena of spontaneous adsorption at solid-liquid interfaces, there is no unified theory that quantitatively describes how it occurs [54–56]. The process is complex and is of practical importance across a wide range of applications, including biomaterials, biosensing and fluidic devices. In all of these contexts, nonspecific adsorption will influence performance by altering surface properties, fouling interfaces or perturbing analyte behavior.

At a fundamental level, adsorption is governed by a balance of thermodynamic contributions, where spontaneous adsorption will occur only if there is a reduction in the Gibbs free energy, ΔG_{ads} [57],

$$\Delta G_{ads} = \Delta H_{ads} - T\Delta S_{ads}, \tag{3.1}$$

where ΔH_{ads} is the enthalpic change and ΔS_{ads} is the entropic change. Here, both enthalpic and entropic contributions arise from multiple interacting mechanisms, involving both the particle, the interface and the surrounding solvent. Rather than being dominated by a single interaction, adsorption results from an interplay and balance between electrostatic interactions, hydrophobic effects, hydrogen bonding, van der Waals forces and structural rearrangements. Some of these are schematically illustrated in **Figure 3.2**. This section will detail these interactions, first from the perspective of protein adsorption and later extended to larger biological nanoparticles (BNPs).

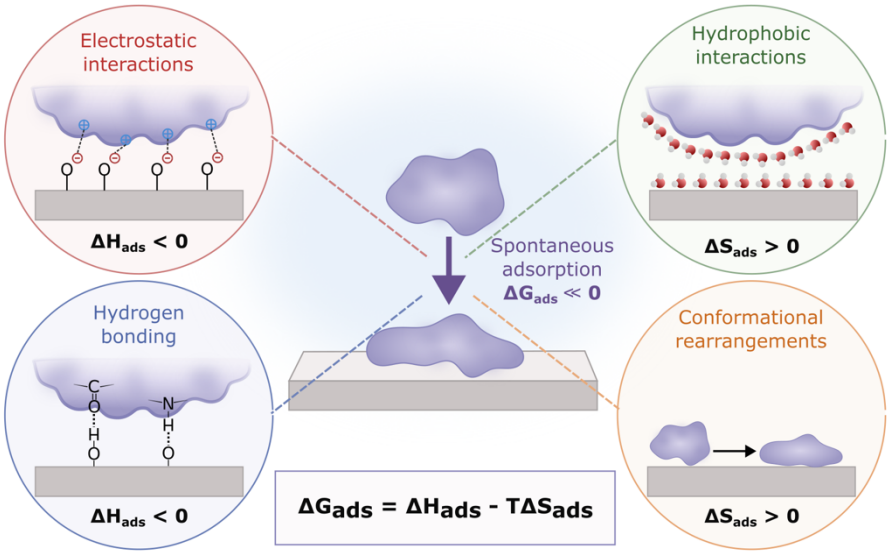

Figure 3.2 Schematic summary of mechanisms involved in the nonspecific adsorption of proteins at solid-liquid interfaces. *Spontaneous adsorption occurs when there is a reduction in Gibbs free energy (ΔG_{ads}) from enthalpic contributions, such as electrostatic interactions and hydrogen bonding, and entropic contributions, such as release of structured water in hydrophobic interactions and protein conformational rearrangements upon adsorption.*

3.1.1 Adsorption of proteins

Electrostatic interactions

Proteins in aqueous solution typically carry a net charge determined by the relation between their isoelectric point and the solution pH[54,58]. At a pH > pI, proteins are negatively charged, while at pH < pI they carry a net positive charge. Similarly, silica surfaces are negatively charged at neutral pH due to deprotonated surface silanol groups, and thus there is potential for electrostatic interactions between the two.

Electrostatic interactions between proteins and surfaces contribute significantly to the enthalpic term of adsorption and lower the system enthalpy when the charges are opposite, favoring adsorption[57]. In addition, both surfaces are surrounded by electrical double layers (EDLs). Hence, when two surfaces approach each other, overlap of these layers leads to ion redistribution and release to maintain charge neutrality at the interface, which will contribute to the system's entropy[57,58]. The range of these electrostatic interactions is governed by the Debye screening length and decreases with the ionic strength of the solvent[54]. Electrostatic interactions will thus depend on both the solution pH and ionic strength[57,59].

Importantly, the overall protein and surface charge alone are not enough to determine adsorption behavior. Proteins with the same net charge as the surface may still adsorb[57,58,60], as exemplified by bovine serum albumin on silica[59]. This can be explained by the heterogeneous distribution of charge on the protein surface, where localized oppositely charged patches can interact favorably with the surface. Adsorption is therefore governed by local interaction, rather than the overall net charge.

Hydrophobic interactions

Hydrophobic interactions arise from the ordering of water molecules around non-polar regions, which reduces the system's entropy[57,60,61]. When hydrophobic regions are brought into contact, such as when two surfaces interact, this ordered water is released back into the bulk, increasing the entropy of the system. This provides a driving force for adsorption, particularly for a hydrophobic surface, where this effect can outweigh that of electrostatic repulsion[55].

While this effect is strongest for adsorption on hydrophobic surfaces, it also plays a role in the interaction of amphiphilic proteins with hydrophilic surfaces, such as silica that I use in this thesis. Specifically, returning to the example of BSA adsorption on silica[59], the hydrophobic domains of the protein will influence how it approaches and orients at the interface, even if final interactions occur via hydrophilic or charged residues. In this way, hydrophobic interactions contribute to the initial adsorption process and further stabilize the adsorbed state, as the protein rearranges to minimize the exposure of the hydrophobic domains to the surrounding water.

Conformational rearrangements and protein properties

In aqueous solution, proteins adopt folded conformations that minimize free energy, largely driven by the hydrophobic effect which shields non-polar residues from the surrounding environment[57]. The folded state contains regions of ordered secondary structures, such as α-helices and β-sheets, which are further stabilized by hydrogen bonds between peptide groups. However, the formation of these ordered structures reduces the conformational entropy and restricts rotational mobility around the polypeptide backbone. As a result, the folded structure can easily be perturbed by changes in environmental conditions.

Introducing a solid surface into the system shifts the balance of interactions, as the free energy minimum of the adsorbed state differs from that in bulk solution[54]. Upon adsorption, the protein may undergo conformational rearrangements to increase its interaction with the surface, exposing previously buried hydrophobic regions that stabilize secondary structures[54,57]. In some cases, this entropic gain can compensate unfavorable

electrostatic and dehydration effects, making adsorption favorable even under seemingly repulsive conditions[60,62].

The extent of these conformational rearrangements depends on the protein's intrinsic stability[54,57,58]. Based on this, proteins are often classified as either "hard" or "soft" proteins. Hard proteins, with rigid, stable structures, undergo limited conformational changes and are less likely to adsorb to hydrophilic surfaces unless there is an electrostatic driving force. In contrast, "soft" proteins possess lower structural stability and are more prone to adsorption on both hydrophilic and hydrophobic surfaces. Finally, as the structural changes may also increase the number of contact points with the surface, the adsorption can become effectively irreversible[58]. The induced conformational change may or may not persist as the protein eventually desorbs from the surface[54,62].

Hydrogen bonding

Hydrogen bonding can occur between functional groups on the surface and the protein, for example, between silanol groups on silica and carbonyl or amide groups in proteins[58]. However, the net contribution of hydrogen bonding to adsorption is often limited, as newly formed bonds typically replace pre-existing hydrogen bonds with surrounding water, leading to only a small overall enthalpic gain[57].

3.1.2 Adsorption of biological nanoparticles

The same fundamental interactions described above also influence the adsorption of larger biologically relevant nanoparticles including liposomes, lipid nanoparticles (LNPs) and extracellular vesicles (EVs)[63]. As these particles are of increasing interest in both biotechnology and medicine, for

example as drug delivery vehicles[24,64,65] and biomarkers[23], control of nonspecific adsorption is therefore relevant in both analytical and applied contexts such as NSM characterization attempted in this thesis.

Most understanding of the adsorption of lipid-based particles at solid-liquid interfaces stems from model systems such as synthetic liposomes. Unlike proteins, these particles are soft and deformable, introducing an additional balance between surface adhesion energy and the energetic cost of membrane deformation upon contact with the interface[66]. Upon adsorption, vesicles may remain intact, deform, or rupture to form supported lipid bilayers (SLBs), depending on factors such as lipid composition, pH, ionic strength and the presence of multivalent ions, as well as the substrate properties[63,66–70].

EVs share this membrane-bound architecture but are structurally more complex, with heterogeneous surfaces composed of lipids, proteins, and glycans and they are often further modified by a protein corona in biological fluids[71]. Although EVs typically carry a negative net charge under physiological conditions, they are still prone to adsorption on silica subtrates[72–74]. As for proteins, this can be understood in terms of local interactions, surface heterogeneity and deformations at the interface which can overcome electrostatic repulsion and stabilize the adsorbed state.

LNPs differ structurally from both liposomes and extracellular vesicles in their internal organization, which is composed of ionizable lipids, helper lipids, cholesterol and encapsulated cargo[24]. Furthermore, to maintain colloidal stability and in vivo circulation, they are typically formulated with PEGylated lipids. While direct studies of LNP adsorption to solid substrates is limited, PEGylated liposomes can be explored as model systems[75].

Interestingly, the PEG chains can exhibit affinity for silica surfaces, promoting particle adsorption through interactions with surface silanol groups. This suggests that PEGylation, while preventing particle aggregation in bulk, may not fully suppress particle-surface interactions. This is relevant in the context of **Manuscript II**, where we characterize LNPs using NSM.

3.1.3 Summary

Overall, adsorption at solid-liquid interfaces can in most cases not be attributed to a single dominant mechanism. Instead, it results from a complex interplay of multiple contributions to the free energy, which vary with the analyte and environmental conditions. Systems that may be expected to resist adsorption to silica surfaces based on electrostatic interactions, may still show non-specific adsorption due to local interactions, molecular/particle heterogeneity and structural/mechanical rearrangements at the interface. As discussed next, in nanofluidic systems, these effects are further amplified by confinement, increasing the frequency of particle-surface encounters, posing a fundamental challenge for the reliable characterization of particles using NSM.

3.2 Adsorption in Nanofluidic Systems

When describing nonspecific adsorption of biological analytes to surfaces, it is important to consider not only the nature of the intermolecular interactions involved, but also the frequency with which particles encounter the surface in the first place. In confined systems, this encounter frequency is fundamentally altered by geometry.

As the confinement increases, the surface-to-volume ratio increases, and the average distance between particles enclosed in the volume and surrounding surfaces decreases. For example, the surface-to-volume ratio of 50 x 50 nm^2, the smallest nanofluidic channels used in this thesis, is 2-3 orders of magnitude larger than that of a typical microfluidic channel (10-100 μm in characteristic length)[76] used for bioanalytical applications. This geometric scaling alone suggests that particle-surface interactions will be more frequent in nanofluidic systems[77,78], as conceptually illustrated in **Figure 3.3**.

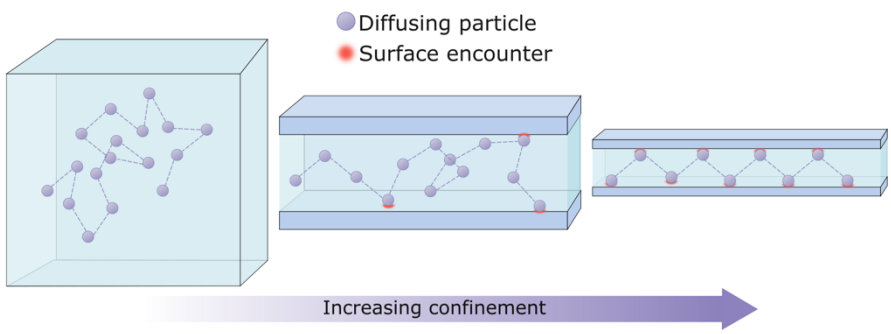

Figure 3.3 Conceptual illustration of how increasing confinement influences particle-surface encounters. *As the dimensions of the system decrease from bulk to micro- and nanofluidic scales, the surface-to-volume ratio increases, leading to more frequent encounters between diffusing particles and the confining walls.*

To quantify the increased frequency with which a particle will encounter the surface, a first passage time approach can be used[79,80]. This framework describes the average time required for a diffusing particle to reach a boundary for the first time. Considering a one-dimensional system on the interval $[0, L]$, where the boundaries represent the channel walls, the mean time, t, it will take for a particle at the initial position x_0 to reach either wall[79,80] is

$$t(x_0) = \frac{x_0(L - x_0)}{2D}, \tag{3.2}$$

where D is the particle diffusion coefficient. Averaging over a uniform distribution of initial positions, the spatially averaged mean first passage time is given by

$$\langle t \rangle = \frac{1}{L}\int_0^L t(x_0)\, dx_0 = \frac{L^2}{12D}, \tag{3.3}$$

showing a quadratic dependence on the confinement length scale. Comparing characteristic dimensions, this scaling implies that a particle diffusing in a 50 x 50 nm^2 nanochannel will encounter a wall $\frac{\langle t \rangle_{\text{micro}}}{\langle t \rangle_{\text{nano}}} \sim 10^6$ times more frequently than in a 100 x 100 μm^2 microfluidic channel.

However, the above treatment assumes a point-like particle. In reality, particles have a finite size, which introduces additional steric confinement. Hence, the accessible length for the particle center is reduced to,

$$L_a = L - 2r_p, \tag{3.4}$$

due to the center of the particle not being able to approach the surface closer than its radius, r_p. Replacing L in Eq 3.3 with the expression for L_a introduces two size-dependent effects that become significant when the confinement ratio r_p/L is no longer negligible. When the particle size increases, the diffusion coefficient decreases according to the Stokes-Einstein relation, which increases the mean first passage time. Simultaneously, the accessible

diffusion space decreases since the particle center cannot approach the wall closer than one particle radius, thereby shortening the distance required to encounter the surface and reducing the first-passage time. In bulk systems, $r_p \ll L$, and the effect is negligible. As shown in **Figure 3.4**, this leads to a deviation from the simple point-particle scaling and can, depending on the ratio r_p/L, result in more frequent surface encounters. The curves in **Figure 3.4** have been calculated for a characteristic channel width/height (i.e distance L) of 300 nm, representative of the channels used in this thesis for the characterization of liposomes and LNPs.

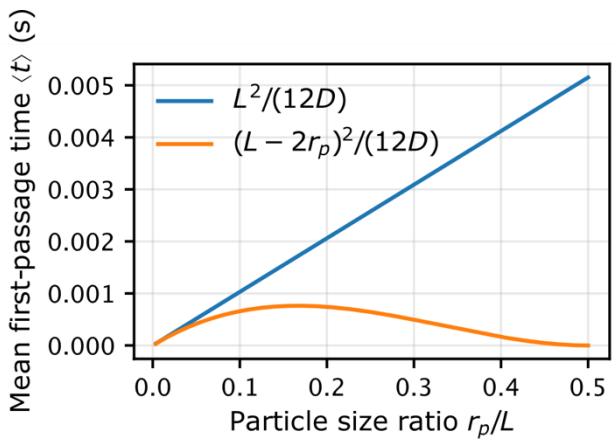

Figure 3.4 Mean first-passage time $\langle t \rangle$ to the channel wall as a function of particle size ratio r/L. *The blue curve shows the point-particle scaling, where increasing particle size leads to increase in $\langle t \rangle$, due to the reduced diffusivity D. The orange curve represents the sterically corrected case, where an increase in particle size will reduce the accessible space, leading to a competing effect that decreases $\langle t \rangle$.*

It should be noted that this simplified description neglects additional confinement effects. Hydrodynamic interactions with the channel walls reduce the effective diffusivity relative to bulk conditions[39], and electrostatic

interactions may further influence particle-surface interactions depending on the ionic strength of the solution[77,81]. Under the physiological conditions used in this thesis (150 mM salt concentration), the Debye screening length is ~1 nm indicating that electrostatic interactions are short-ranged. Nevertheless, confinement still strongly increases the frequency of particle-surface encounters and consequently, the opportunity for non-specific adsorption.

Having now described how non-specific adsorption arises from intermolecular mechanisms and system-specific properties and how it may be amplified by geometrical confinement, the next section will focus on strategies to mitigate these effects.

3.3 Strategies for Mitigating Nonspecific Adsorption

Since nonspecific adsorption of biological nanoparticles and the resulting surface fouling are widespread challenges in applications such as bioanalytical devices and medical implants, significant effort has been devoted to developing surface passivation strategies. Although different approaches rely on different chemistries their effectiveness is generally rooted in a common set of structural features.

In general, non-fouling surfaces combine three key features: i) strong surface hydration, ii) steric and entropic repulsion that counteracts particle approach, and iii) overall electrical neutrality[82,83]. Among these, surface hydration is considered to be dominant. When two (hydrophilic) surfaces approach in aqueous environments, removal of tightly bound interfacial water is associated with a free energy penalty, giving rise to short-range repulsive forces commonly referred to as hydration forces[84]. Functional groups that

strongly interact with water therefore promote the formation of a stable hydration layer that acts as an energetic barrier to protein adsorption[82,85,86].

In addition, steric repulsion plays an important role, particularly for polymer-based passivation strategies. When polymer chains are tethered to a surface, they extend into the surrounding solution, forming a brush-like layer [87,88]. Beyond simply acting as a physical barrier between the particle and the surface, compression of these chains upon particle approach leads to a loss of configurational entropy, resulting in a repulsive contribution to the free energy that further suppresses adsorption[82,89,90]. Finally, maintaining overall charge neutrality reduces attractive electrostatic interactions between the surface and charged particles[84,91].

Together, these mechanisms form the basis for the design of antifouling surfaces. In the following sections, common approaches are outlined, focusing on zwitterionic coatings, supported lipid bilayers and hydrophilic brushes, where the PLL-g-PEG approach used in **Manuscript I** belongs to the latter.

Zwitterionic materials

A zwitterion is an ionic compound containing equal numbers of positively and negatively charged groups[92]. In antifouling materials, this makes them especially interesting as they can strongly bind to water through electrostatically induced hydration, while maintaining an overall net neutral charge[82]. Polyzwitterions are the polymeric analogues in which the ionic groups are arranged along the polymer backbone, either within the same monomer unit (polybetaines) or distributed across different monomers (polyampholytes). Polybetaines are further classified based on the chemical

nature of the negatively charged group, including sulfonate, carboxylate and phosphate. As such, zwitterionic polymers are a large and diverse class of materials, where variations in charge type, charge density, spatial separation of ionic groups and polymer architecture can be tuned to enhance antifouling performance[93].

Lipid bilayers

Supported lipid bilayers (SLBs) can be viewed as a biomimetic extension of zwitterionic and have long been used as model systems for biological membranes[94]. Cell membranes have an inherent resistance to nonspecific adsorption, partly attributed to the hydrophilicity of the structural phospholipids[95], particularly phosphatidylcholine (PC) which is abundant in eukaryotic cells membranes[96]. Accordingly, SLBs based on PC lipids have been shown to suppress nonspecific adsorption[97,98].

SLBs are commonly formed via vesicle fusion, where lipid vesicles adsorb, rupture and spread to form a continuous bilayer[98]. This approach has also been implemented in nanofluidic systems, including NSM, where POPC vesicles were ruptured in the microchannels and allowed to spread into the nanofluidic channels[20,78]. However, the applicability of this approach becomes increasingly limited as channel dimensions decrease. For nanochannels with cross-sectional dimensions of 80 x 40 nm^2, the process required 12 h, with periodic and careful flow control to avoid channel clogging[20]. Combined with the need for vesicle preparation prior to each experiment, this limits the practicality of SLBs for routine NSM applications.

Hydrophilic PEG-based coatings

Hydrophilic polymer coatings represent a second major class of antifouling materials, among which polyethylene glycol (PEG) is one of the most widely used[82,99]. The antifouling properties of PEG arise form a combination of surface hydration and steric repulsion. The ether oxygen groups along the PEG backbone act as hydrogen bond acceptors, promoting the formation of a hydrated layer, while the conformational flexibility of the polymer leads to steric and entropic repulsion upon compression[82,100].

An effective antifouling behavior requires high surface density of tethered polymers such that the polymers adopt an extended brush-like conformation[87,88]. This can be achieved using a grafting-from approach, for example via atom-transfer radical polymerization[101,102], where polymers are grown bottom-up from a surface immobilized initiator. However, in the context of nanofluidic channels, this approach would be experimentally demanding as it requires an initial homogeneous initiator monolayer, oxygen-free polymerization conditions and controlled reagent delivery – all within confined geometries.

An alternative is the grafting-to approach, where preformed polymers are transported and covalently attached to the surfaces[103–105]. For silica substrates, this typically relies on silane chemistry, where organosilanes react with surface silanol groups to form the anchoring layer. However, silanization reactions are sensitive to moisture and prone to side reactions such as premature hydrolysis and cross-linking, which can compromise the formation of a uniform monolayer[103]. As a result, silanization protocols often require the use of dry organic solvents and strict control of surface hydration,

which can complicate reproducibility[103,104]. These conditions are particularly challenging to control in enclosed nanofluidic systems.

Covalent PEG attachment in silica-based nanofluidic devices has been demonstrated using a multistep grafting-to protocol, herein referred to as APS-SMCC-PEG functionalization[106]. In this approach, a monolayer of 3-aminopropylsilatrane (APS) is first formed on the surface, followed by the click coupling of a sulfo-SMCC linker, and finally attachment of thiol-terminated PEG. Compared to conventional silanes, the silatrane precursor has improved stability in hydrous environments due to its compact and closed structure, enabling more controlled surface functionalization. The resulting layer is a dense PEG coating formed *in situ* within the nanochannels by sequential rinsing of the respective chemicals, as shown in **Figure 3.5a**.

The APS-SMCC-PEG protocol was initially considered as a candidate for routine use in NSM experiments and we found it to perform well for nanochannels down to ~ 100 x 100 nm^2, which enabled measurement of BNPs, as exemplified by the kymograph in **Figure 3.5b.** However, several practical limitations became apparent. First, the protocol relies on in-house synthesis of the APS precursor, as it is not readily commercially available. In addition, the limited solubility of the SMCC linker in aqueous solution led to the formation of aggregates, which were prone to clogging the nanochannels. Furthermore, to avoid cross-linking of reactants in solution, the fluidic system, including sample reservoirs, has to be thoroughly rinsed between steps, making the protocol labor intensive and time-consuming. In the end, the protocol has found a place in the "NSM toolbox", as it still offers the advantage of covalent attachment. However, these ease-of-use limitations motivated the search for an even simpler passivation method.

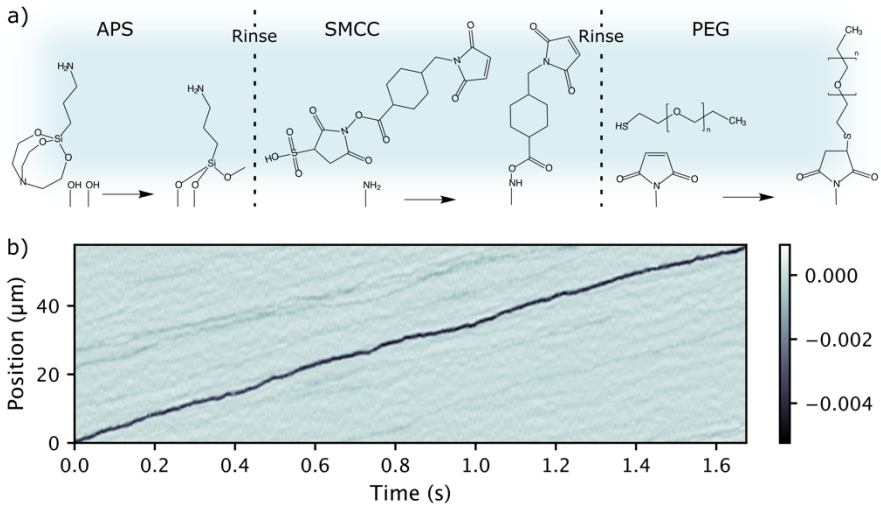

Figure 3.5 Passivation using APS-SMCC-PEG. *a) In situ functionalization of nanochannels by sequential flushing of each chemical, with intermediate rinsing steps. b) Processed kymograph showing the measurement of an extracellular vesicle, enabled by APS-SMCC-PEG passivation.*

PLL-g-PEG coatings

An alternative to covalent attachment is physisorption, which reduces the requirements of surface preparation and reaction control. In the case of PEG, this can be achieved by grafting PEG chains onto a polyelectrolyte backbone, enabling physisorption via electrostatic interactions. This is the basis of PLL-g-PEG based coatings, a well-established class of antifouling graft copolymers for metal oxides and silica surfaces[107–110]. The general structure of these copolymers is shown in **Figure 3.6**.

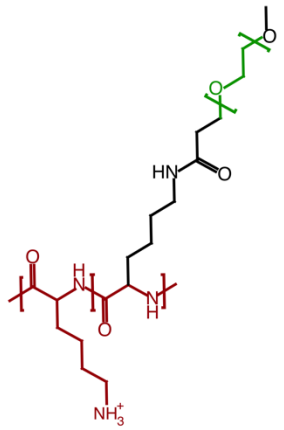

PLL-g-PEG

Figure 3.6 General chemical structure of PLL-g-PEG graft copolymers. *Red highlights the PLL backbone and green highlights the PEG chains. The polymer electrostatically binds to oxide surfaces via the protonated primary amine on the PLL backbone.*

Electrostatic adsorption of PLL-g-PEG to negatively charged oxides is driven by the positively charged PLL backbone, due to the presence of protonated amine groups, leading to rapid and spontaneous assembly from aqueous solutions[107,108]. The resulting layer adopts a comb-like structure, with the PLL backbone adsorbed parallel to the surface and PEG chains extending into solution, perpendicular to the surface[108]. This configuration forms a highly hydrated, brush-like layer that provides both hydration and steric repulsion and direct force measurements have shown that these layers behave as elastically compressible polymer brushes, with a measured water content exceeding 80%[110].

PLL-g-PEG coatings exhibit strong resistance to nonspecific adsorption of proteins and to complex media such as blood serum and plasma[107,111]. Their performance will depend on the surface density of the ethylene glycol units, which is controlled by PEG chain length and grafting ratio[109]. The variant used in this thesis, PLL(20)-g[3.5]-PEG(2), has been identified as an effective compromise between strong surface anchoring and sufficiently dense PEG coverage[107,109]. The adsorption of PLL-g-PEG occurs over a broad pH window of 3-11 and at ionic strengths below ~2 M[107]. Once formed, the adsorbed layer remains stable over extended periods under flow conditions. Furthermore, the adsorption process and performance are retained even in the presence of surface contaminants[107].

Beyond these fundamental studies, PLL-g-PEG coatings have been implemented in systems such as nanopores[112], PDMS-based microfluidic devices[113] and nanoslits[114], and today, the platform is commercialized by SuSoS. Importantly, the resulting layer is thin (~ 5 nm for PEG 2 kDa[115]) and therefore compatible with nanofluidic confinement. Taken together, this makes PLL-g-PEG well suited for surface passivation of our nanofluidic systems, as demonstrated in **Manuscript I**.

3.4 PLL-g-PEG Passivation for NSM

PLL-g-PEG surface passivation in nanofluidic chips can be performed entirely in situ under mild, aqueous conditions which makes it easy to integrate with the NSM workflow. The protocol, summarized schematically in **Figure 3.7a** consists of a simple sequence of rinsing, buffer equilibration (50 mM HEPES, pH 7.4), and introduction of the PLL-g-PEG solution, followed by removal of excess polymer, leaving the nanochannels ready for

immediate experiments. This straightforward procedure enables rapid preparation of passivated nanochannels, without requiring complex surface chemistry and complex passivation conditions.

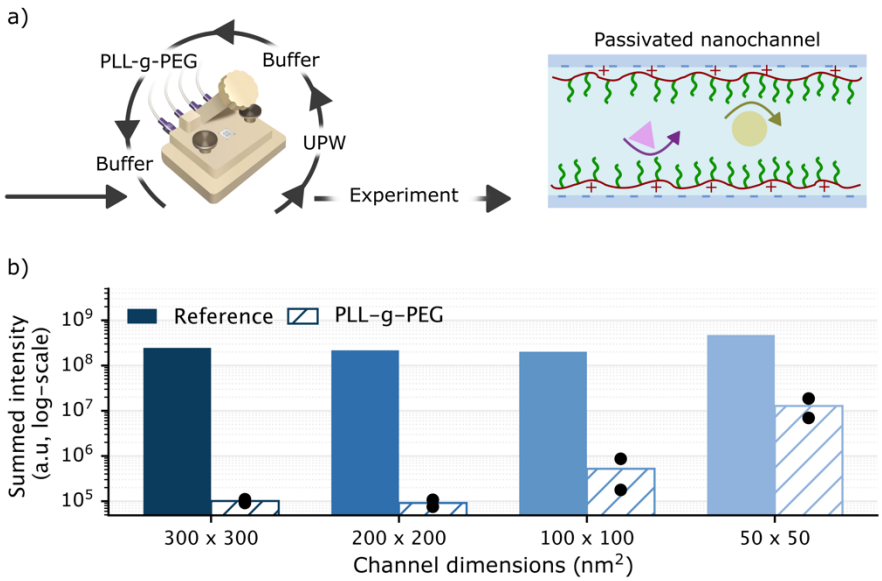

Figure 3.7 Procedure for in situ PLL-g-PEG passivation. a) *The nanofluidic chip is passivated mounted on the microscope by sequential rinsing of ultrapure water (UPW), passivation buffer and PLL-g-PEG solution. Remaining polymer is rinsed out after completed passivation and subsequent experiments can be performed.* **b)** *Integrated fluorescent intensity after incubation with avidin-FITC, showing reduced adsorption in PLL-g-PEG passivated nanochannels. Bars show the mean of two individual replicate. The individual replicates are shown as scattered black points.*

The effectiveness of the passivation was first evaluated using a fluorescence assay, in which FITC-labeled avidin was introduced into the channels and the resulting fluorescence signal after incubation was compared with that of

non-passivated references (**Figure 3.7b**). A suppression of fluorescent intensity of 1-3 orders of magnitude was observed across a range of channel dimensions, demonstrating a substantial reduction of nonspecific adsorption. A small, residual signal remained in the most confined 50 x 50 nm^2 channels, highlighting the challenges of effective passivation layers under extreme confinement. Important to note however, is that the fluorescent signal was still suppressed by up to 97%.

The impact of passivation was further assessed in NSM measurements. The PLL-g-PEG coating enabled reliable characterization of liposome size in the larger 300 x 300 nm^2 channels and improved the accuracy of size and molecular weight determination for apoferritin proteins in smaller, 100 x 50 $nm^{2,}$ channels (**Figure 3.8**). This demonstrates that suppression of nonspecific adsorption is essential for obtaining accurate diffusion-based measurements, and that surface passivation extends the applicability of NSM to a broader range of particle types and channel dimensions.

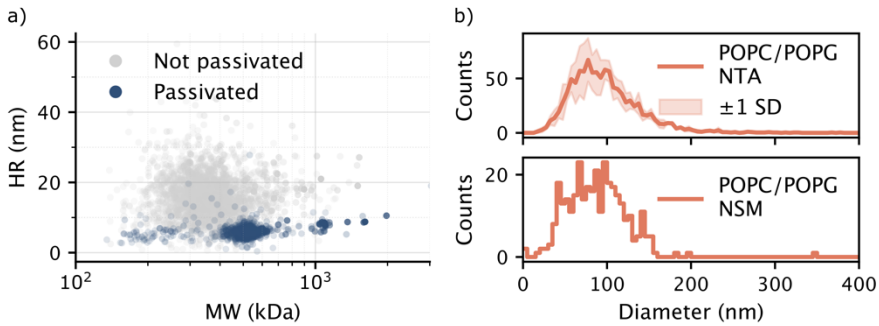

Figure 3.8 NSM measurements improved by PLL-g-PEG passivation. a) *Scatter plot of hydrodynamic radius (HR) vs molecular weight (MW) in PLL-g-PEG passivated and non-passivated channels. The passivation reduced the spread of both dimensions, thereby enabling more precise and accurate characterization.* **b)** *NSM histogram of inferred liposome diameter as measured in PLL-g-PEG passivated nanochannels, compared with nanoparticle tracking analysis (NTA).*

To further understand the coating process, a fluorescently labeled PLL-g-PEG variant was used to monitor the adsorption *in situ*. This showed a strong dependence of passivation time on channel dimensions: while complete coverage of 100 x 100 nm^2 channels was achieved within minutes, the process required up to 80 minutes for 50 x 50 nm^2 channels. Additionally, the passivation time scaled inversely with polymer concentration. Together, these observations indicate that the coating process is mass-transport limited in confined nanochannels, where the rate of polymer delivery governs the overall adsorption kinetics. This interpretation is further supported by the observation of a sharp adsorption front propagating along the channel (**Figure 3.9**), consistent with a transport-limited regime as opposed to a reaction-limited regime, where a more homogeneous and gradual increase in surface coverage would be expected.

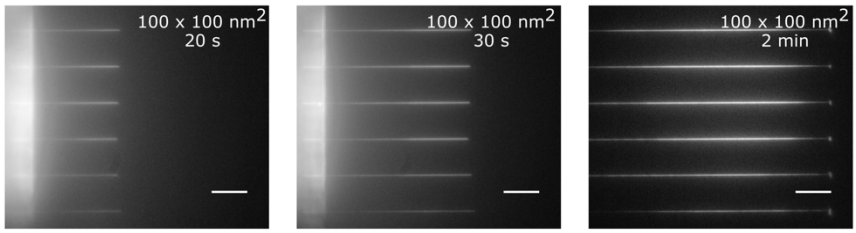

Figure 3.9 Time evolution of passivation front. *Using a fluorescently tagged PLL-g-PEG the passivation can be monitored in situ, here shown for a 100 x 100 nm² channel. The fluorescent micrographs were taken after having stopped the passivation at different time points. Scale bar is 10 μm.*

Finally, although not further explored in **Manuscript I**, the ability to interrupt the coating process at distinct time points provides a mean for spatially controlled surface functionalization. As a proof-of-concept, this is illustrated in **Figure 3.10 (top)**, where a partially passivated nanochannel exhibits a transition in scattering intensity between coated and uncoated regions, analogous to what was observed using the fluorescently tagged PLL-g-PEG. Measurements of apoferritin across this boundary, shown in **Figure 3.10 (bottom)**, show a clear change in behavior: transient surface interactions dominate in the uncoated region, whereas free diffusion is observed in the coated region.

Given that PLL-g-PEG can be modified to exhibit specific binding sites such as biotin[116] or nitrilotriacetic acid[117], while maintaining suppression of nonspecific interactions, this spatial control may enable different regions of the channel to be functionalized with distinct capture chemistries. In this way, a strategy originally developed to solve the issue of nonspecific adsorption in NSM may, perhaps ironically, enable its controlled use,

allowing the platform to evolve from passive characterization into a tool that integrates label-free single-particle detection and imaging with spatially resolved and dynamic analysis of binding interactions.

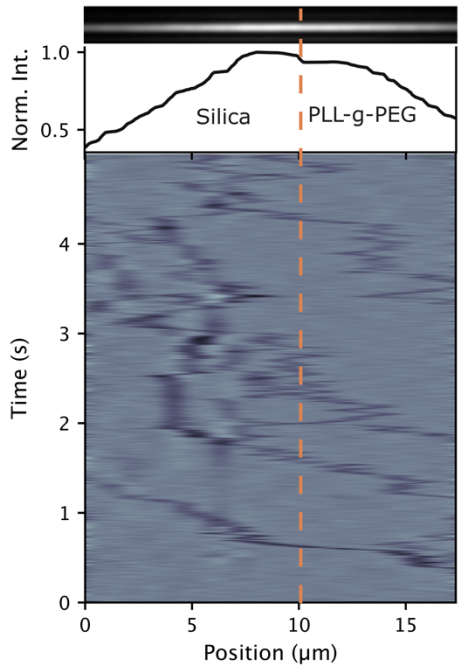

Figure 3.10 Measurement in half-functionalized nanochannel. *PLL-g-PEG functionalization of the nanochannel (dark-field, top) was stopped and the split between uncoated silica PLL-g-PEG coated silica could be identified by a small drop in scattering intensity (middle), as indicated by the dashed line. Measurements of apoferritin carried out at this region (kymograph, bottom) show change in interaction behavior of the protein with the surface.*

4 Lipid Nanoparticle Characterization

In recent years, messenger RNA (mRNA)-based therapeutics have emerged as a promising platform for the treatment and prevention of various diseases[24,25,118]. mRNA molecules are single-stranded ribonucleic acids that serve as templates for translation of the genetic information encoded in our DNA into functional proteins[118]. As mRNA can be synthesized in vitro to encode a specific protein of interest, mRNA therapeutics are attractive for a broad range of applications including vaccination, protein replacement therapies and cancer immunotherapies[24,26]. However, mRNA cannot be directly administered in vivo as it is susceptible to enzymatic degradation in biofluids and the formulation must additionally evade immune clearance, facilitate uptake by target cells and enable escape from the endosome to reach the cytoplasm[24]. Effective cytosolic delivery of mRNA therefore requires a delivery vehicle. Lipid nanoparticles (LNPs) have been developed as the leading non-viral delivery system for this purpose, and they are now used clinically for the delivery of mRNA therapeutics, most notably in the approved COVID-19 vaccines[21,24,26].

The therapeutic performance of LNP formulations is closely dependent on their physicochemical properties, including particle size, size distribution, surface charge, morphology, and encapsulation efficiency, all of which must be carefully characterized and controlled[34,119]. Particle size, in particular, has been shown to influence biodistribution, cellular uptake, and organ-level targeting, making reliable measurement of LNP size distributions essential[32,34]. Encapsulation efficiency is likewise an important parameter, as the RNA concentration is used as a dosing parameter and the amount of RNA

encapsulated within the LNPs influences the therapeutic efficiency[34]. Encapsulation efficiency is most commonly determined using fluorescence-based assays, such as the RiboGreen assay, in which a dye that selectively binds to free mRNA is added to the intact formulation, followed by disruption of the LNPs to release encapsulated cargo, after which the ratio of encapsulated to non-encapsulated mRNA is determined[34,119]. While this approach provides a bulk measurement of the overall fraction of encapsulated cargo within a formulation, it does not provide information regarding the distribution of mRNA between individual LNPs and cannot distinguish between loaded, partially loaded, or empty LNPs[34,120]. However, recent studies have suggested that the fraction of empty LNPs within formulations may be substantial[28,29].

Characterization techniques capable of resolving underlying distributions with respect to both LNP size and loading are therefore of significant interest. In **Manuscript II**, we explored NSM as a platform for label-free single-particle characterization of mRNA-loaded LNPs by investigating twelve different industrially formulated LNP samples. The results were compared with conventional characterization techniques, such as dynamic light scattering (DLS), nanoparticle tracking analysis (NTA) and cryo transmission electron microscopy (cryo-TEM). This chapter will first provide a brief overview of the composition and structure of LNPs, highlighting their complexity and their implications for the interpretation of *iOC* in NSM. Thereafter, conventional techniques used to characterize LNP formulations, employed in **Manuscript II**, will be described. Finally, the main results from **Manuscript II** will be briefly presented.

4.1 Composition and Structure of LNPs

LNPs consist of various kinds of lipids together with the enclosed cargo and are therefore structurally highly complex[121]. Unlike classical liposomes, which consist of an aqueous core enclosed by a lipid bilayer, the core of LNPs is lipid-rich, with lipids organizing around the encapsulated mRNA, adopting multiple coexisting ordered phases[121]. Furthermore, particle morphology may additionally influence the internal structure. In more spherical particles, mRNA tends to be closely associated with the lipid core, whereas in particles that develop bleb-like protrusions due to phase separation between lipid components, mRNA can dissociate from the lipids into aqueous compartments formed in the particle[121,122].

In terms of composition, a typical mRNA-LNP formulation consists of four main lipid constituents: ionizable lipids, helper lipids, cholesterol, and PEG-lipids[21]. The ionizable lipids constitute the largest fraction, comprising 30-50% of the total lipid composition, and their chemical structure directly influences their function due to the pH-dependent ionization of the hydrophilic head-group. As a result, ionizable lipids play different roles throughout the process, from formulation to intracellular delivery[24,25]. At the acidic pH used during formulation, the ionizable lipids carry a positive charge, which enables the electrostatic complexation with the negatively charged mRNA. At physiological pH in the bloodstream, they are instead close to neutral, which reduces interactions with blood cells and improves biocompatibility. Upon cellular uptake through endosomes, the acidic endosomal environment again protonates the ionizable lipids, facilitating endosomal escape and release of the mRNA into the cytosol for subsequent translation.

The helper lipids, which are typically phospholipids and constitute 10-20% of the formulation, contribute to membrane integrity, particle stability, and fusogenicity with target cell membranes[25,123]. Cholesterol, which typically comprises 20-50% of the formulation, is further incorporated to improve membrane rigidity and structural stability by filling spaces between lipids within the particle membrane[25,123]. Finally, PEG-lipids are distributed across the outer particle surface, providing steric stabilization through steric hindrance and preventing the adsorption of plasma proteins onto the particle surface, thereby prolonging the circulation lifetime in the bloodstream[25,26].

The structural and compositional complexity of LNPs described here has important implications for their characterization by NSM. As discussed in **Section 2.3.2**, the interpretation of the measured *iOC* in terms of particle properties relies on assumptions of optical homogeneity and size. For LNPs, the presence of multiple lipid phases and lipid types, aqueous compartments, and nucleic acid cargo means that these systems cannot be described by a single well-defined refractive index. Furthermore, structural heterogeneity between particles within the same formulations, due to differences in cargo loading, lipid phase organization, and morphology, means that the *iOC* distribution measured by NSM for LNP samples is expected to be broad, and its full interpretation remains an open challenge.

4.2 Conventional Techniques for Characterization of LNPs

In **Manuscript II**, twelve different industrially formulated LNPs were investigated and characterized by NSM, with the results benchmarked against conventional methods for LNP size determination. These included

dynamic light scattering, nanoparticle tracking and cryo transmission electron microscopy. This section will provide a brief description of each of these techniques and discuss some important limitations in their ability to characterize LNPs.

4.2.1 Dynamic light scattering (DLS)

DLS is an optical technique widely used for particle size analysis in the submicron range due to its speed, low cost, and ease of use[124]. In a typical DLS measurement, a laser beam is directed through a cuvette containing the sample and the scattered light is collected at a fixed angle. As particles suspended in the solution undergo Brownian motion, they continuously change their relative positions, causing constructive and destructive interference of the scattered light, producing rapid fluctuations in the detected light intensity. The timescale of these fluctuations is related to the particle diffusion rate, with smaller particles producing faster fluctuations. The detected intensity fluctuations are analyzed using an autocorrelation function which quantifies the similarity of the signal at different times and therefore decays as the particles move from their original positions. For smaller particles, the autocorrelation function decays more rapidly than for larger particles, and the decay rate is directly proportional to the particle diffusion coefficient, which in turn is related to the hydrodynamic size through the Stokes-Einstein equation. A consequence of this measurement principle is that larger particles contribute disproportionally to the detected signal, as the scattered light intensity scales with the sixth power of particle size. As a result, DLS produces intensity-weighted distributions, where the reported mean is weighted by scattering intensity rather than by particle number. Besides the hydrodynamic size, DLS also quantifies the polydispersity index (PDI), which represents the width of the distribution.

For LNP formulations intended for biological applications, a PDI below 0.2 is generally considered acceptable[120]. For polydisperse samples, the autocorrelation function consists of several exponential decays and can be decomposed to retrieve underlying size distributions. However, DLS is generally unable to resolve distinct peaks unless they differ in size by approximately a factor of three[124].

The limited resolution for polydisperse samples is problematic for LNP characterization, as the formulations may contain subpopulations of varying size and composition[28,34]. Since larger particles dominate the intensity-weighted signal, smaller particles may be masked and remain undetected, causing DLS to overestimate the mean particle size in polydisperse samples[124,125]. Additionally, the hydrodynamic size derived through the Stokes-Einstein equation assumes spherical particle morphology and therefore may not accurately reflect the true dimensions of aspherical LNPs, such as those exhibiting bleb morphologies[34,124]. Finally, as the technique reports only size-related information, its ability to provide structural and compositional insight into the particles is limited. In summary, while DLS is a valuable tool for routine quality assessment of LNP formulations, these limitations motivate the use of complementary single-particle characterization techniques.

4.2.2 Nanoparticle tracking analysis (NTA)

NTA is a microscopy-based technique that, like DLS, measures the hydrodynamic size of nanoparticles in liquid suspension through their Brownian motion. However, while DLS performs an ensemble measurement, NTA detects and measures particles at the single particle level[126]. In a typical NTA measurement, a laser beam is directed through a

liquid sample, and the light scattered by individual particles is collected through a microscope objective at 90° to the illumination plane. Image analysis algorithms are then used to identify and track individual particles over time, from which the mean square displacement can be determined and translated into a hydrodynamic size via the Stokes-Einstein equation. As each particle is tracked and sized individually, NTA yields number-weighted size distributions rather than intensity weighted distributions, making it less biased towards larger particles than DLS[126]. Additionally, the technique can determine the sample concentration by estimating the number of particles within the observation volume. Beyond size and concentration, NTA can also provide information on the scattered light intensity and can be combined with fluorescence detection to selectively identify and characterize specific subpopulations within complex mixtures[126] .

Despite NTAs advantages over DLS in terms of resolution and single-particle sensitivity, it also has several limitations in the context of LNP characterization. A fundamental constraint of the technique is that its ability to detect particles depend on the amount of light they scatter, which is governed by both particle size and the refractive index contrast between the particle and the surrounding medium[126]. LNPs are soft, lipid-based particles with a refractive index close to that of the aqueous medium in which they are suspended. As a consequence, the smallest detectable LNP size may be considerably larger than the stated lower detection limit of the instrument, which typically refers to high refractive index materials such as gold, and may be as high as 50-60 nm[126]. Smaller LNP populations may therefore fall below the detection threshold and remain undetected, potentially biasing the distribution towards large particles and overestimating particle size[34,125]. Furthermore, while NTA provides number-weighted size distributions and

can better resolve polydisperse samples compared to DLS, the technique requires careful optimization of instrument settings, and the results can be highly sensitive to the choices made by the operator[125,126]. Finally, similar to DLS, NTA reports only the hydrodynamic diameter and cannot provide compositional or structural information about individual particles, unless used in the fluorescence mode with specific labels.

4.2.3 Cryo Transmission Electron Microscopy (Cryo-TEM)

In conventional TEM, imaging is performed under vacuum to avoid collisions between the electrons and the atmosphere. For hydrated samples however, this causes severe structural changes and shrinkage, and the imaged structure may bear little resemblance to the hydrated morphology[127]. Cryo-TEM instead preserves sample structure through vitrification, in which the sample is frozen at a sufficiently high rate for the surrounding water molecules to become locked into an amorphous, glass-like state[127]. Sample preparation for cryo-TEM imaging involves applying a small aliquot of the liquid suspension onto a carbon-coated TEM grid, followed by blotting with filter paper to produce an ultra-thin film of approximately 100 nm in thickness. The grid is then rapidly plunged into liquid ethane, after which the vitrified sample is ready for imaging[127]. Within the vitreous ice, the particles are essentially preserved in their native state, allowing morphological features such as shape, size, internal structure, and distinct populations to be observed at high spatial resolution[127]. For LNPs specifically, cryo-TEM has played a role in revealing the characteristic lipid-rich core structure, visualizing the non-spherical bleb morphologies, and identifying coexisting lipid phases within individual particles[34,121].

Despite its powerful imaging capabilities, cryo-TEM has several important limitations in the context of routine LNP characterization. A practical limitation is that the technique requires labor-intensive and technically demanding sample preparation while simultaneously having inherently low throughput[34,127]. The latter is particularly important, as it may compromise the statistical representativeness of the resulting size distributions. Furthermore, preparation of the ultra-thin film may introduce a size bias, as structures exceeding the film thickness can be removed or displaced during blotting, thereby skewing the size distribution towards smaller particles[127]. Finally, while cryo-TEM provides detailed morphological information, the inherently low contrast of unstained vitrified particles can make it difficult to distinguish between different lipid phases or to localize nucleic acid within the particle[34,121,127]. To address this, staining agents such as the cationic thionine dye can be used as an mRNA-specific contrast agent, enabling more precise localization of mRNA within individual LNPs[122].

In **Manuscript II**, cryo-TEM was used to image a subset of the investigated LNP samples, as shown in **Figure 4.1**. The imaging was performed primarily to determine the size distributions of four different formulations (labeled S1, S2, S9 and S11). However, clear morphological differences between the samples were also observed. For example, S1 exhibited highly spherical structures, whereas S9 showed pronounced blebbing (as indicated by the arrow in **Figure 4.1**). Sample S11 appeared to be of lower structural quality, showing fragmented particle structures.

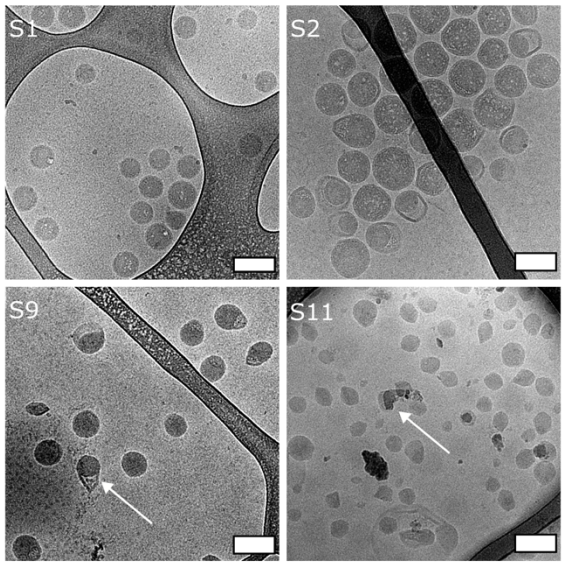

Figure 4.1 Cryo-TEM characterization of lipid nanoparticles. *Representative cryo-TEM micrographs taken for four different LNP formulations, labeled S1, S2, S9 and S11. Cryo-TEM enables single-particle analysis of LNP morphologies, and the arrows in S9 and S11 indicate the presence of aspherical bleb-like structures and degraded sample, respectively.*

4.3 Characterization of LNPs with NSM

Twelve different LNP samples (S1-S12) were investigated in **Manuscript II**, all of which were industry-grade formulations. Furthermore, all formulations contained the same ionizable lipid, but differed in their overall composition with respect to the relative ratios of the lipid constituents. The LNPs were measured in nanochannels with cross-sectional dimensions of 300 x 350 nm^2, and the PLL-g-PEG passivation strategy described in **Chapter 3** was used to mitigate non-specific adsorption events, thereby enabling estimation of hydrodynamic size.

We first investigated the inferred median sample diameter measured by NSM and compared it with the corresponding values obtained by DLS and NTA, as shown in **Figure 4.2**. The samples were measured twice using NTA, on different instruments and by different operators, and the two measurements yielded different characteristic sample diameters, which is a known limitation of NTA, as discussed above. Nevertheless, an overall trend across the samples can still be observed, which NSM is likewise able to capture. Furthermore, NSM systematically reported lower characteristic sample diameters, differing by ~ 10 nm. This is not entirely unexpected, as both DLS and NTA both have reduced sensitivity towards smaller particles present in the sample, as discussed previously, and may therefore overestimate the LNP size. This observed difference may thus indicate an advantage of NSM in its sensitivity towards the smaller size regime.

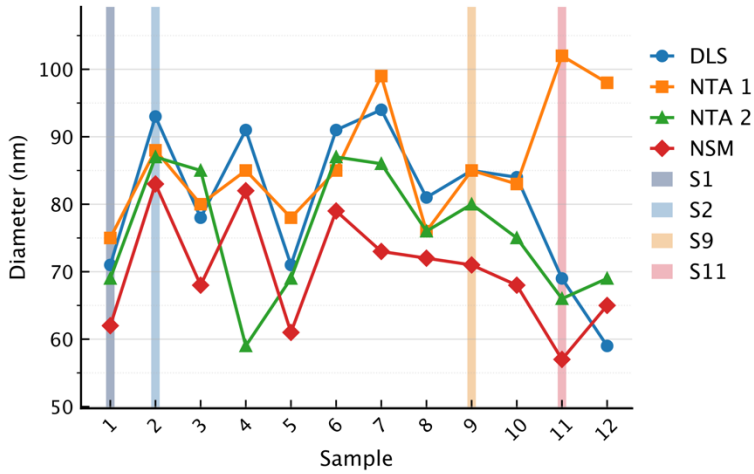

Figure 4.2 Comparison of inferred LNP diameter across samples. *The inferred sample diameter as reported by DLS, NTA and NSM. For NSM and NTA the median diameter is reported, whereas for DLS the distribution mean is reported. NSM can capture the overall trend across all twelve samples, while systematically inferring smaller diameters compared to DLS and NTA.*

Next, four samples (S1, S2, S9 and S11) were selected for a more detailed investigation of the underlying size distributions and to compare the distributions resolved by NSM with those obtained by NTA and cryo-TEM. These results are shown in **Figure 4.3**. When comparing NSM and NTA (**Figure 4.3a**), the distributions can be seen to overlap relatively well. However, the NTA distributions exhibit a tail towards larger diameters, which is particularly pronounced for sample S1 and S11. This may reflect the inherent bias of NTA toward larger particles. However, it may also indicate size filtration effects due to the nanochannels in NSM, as discussed in **Chapter 2**, where rare large-particle subpopulations may become underrepresented due their increased difficulty in entering the nanochannels.

To establish NSM as a reliable platform for the characterization of biological nanoparticles, this effect will have to be investigated in greater detail.

The NSM size distribution was also compared to the distribution derived from cryo-TEM imaging of the LNP samples, and the comparison is shown in **Figure 4.3b**. From these distributions, it is evident that the NSM distributions are instead shifted toward larger particle diameters, with differences in median diameter across the samples on the order of 10 nm. Part of this discrepancy can be explained by the different size parameters used to characterize the particles. In NSM (as well as DLS and NTA), the inferred parameter is the hydrodynamic diameter, whereas the geometric diameter is extracted from the cryo-TEM micrographs. The hydrodynamic diameter includes contributions from associated hydration layers and, for these LNP formulations, the PEG layer present on the particle surface. These polymers are not captured in TEM images due to their low contrast and therefore do not contribute to the inferred particle diameter[128]. Furthermore, it is possible that the smallest particles within the LNP samples remain undetected in NSM due to the relatively large nanochannels used in this study. However, since the detection limit in NSM is determined by the cross-sectional area of the nanochannel cross-sectional dimensions, this limitation can be addressed through the use of smaller channels. Finally, as discussed in greater detail in **Manuscript II**, distribution characteristics such as span and PDI, were found to be similar for NSM and cryo-TEM, indicating that despite the systematic shift in diameter, NSM is still able to capture the overall distribution characteristics of the LNP samples.

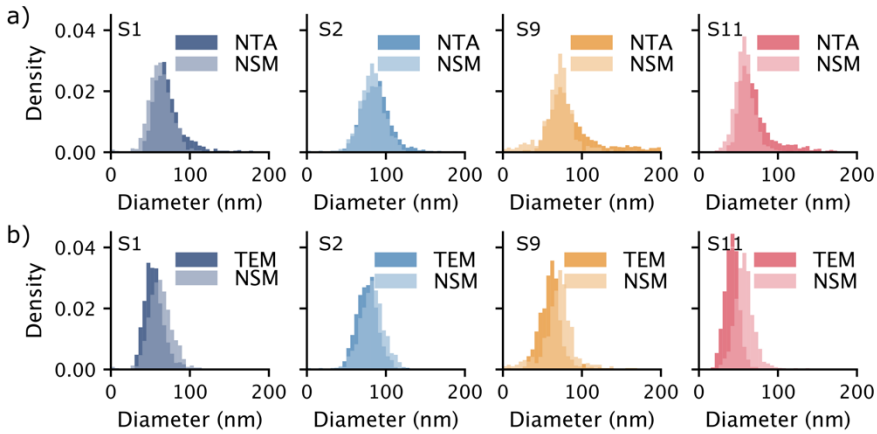

Figure 4.3 Comparison of NSM size distributions with NTA and cryo-TEM. ***a)*** *Histograms of inferred hydrodynamic diameter by NSM and NTA for samples S1, S2, S9 and S11.* ***b)*** *Histograms of inferred diameter by NSM (hydrodynamic) and TEM (geometric).*

As a final part in this study, the second NSM descriptor, *iOC*, was also included in the analysis to investigate whether it could provide additional information regarding particle optical properties. As the *iOC* is dependent on both particle polarizability and particle volume, any observed intra- and inter-sample differences in *iOC* may reflect differences in particle size, optical density or both. Since particle size is determined orthogonally from the *iOC* in NSM, the *iOC* can be normalized to particle volume, V_p,

$$\frac{iOC}{V_\mathrm{p}} = 3\frac{\bar{n}}{A}\frac{n_{\mathrm{p,eff}}^2 - n^2}{2n^2 + n_{\mathrm{p,eff}}^2}, \tag{4.1}$$

yielding a parameter, iOC/V_p, which is more directly related to the particle optical properties through the effective refractive index, n_eff. The result of

this analysis across the twelve LNP samples are shown in **Figure 4.4** in the form of violin plots. Across the samples, the trend in the median $-iOC/V_p$ was observed to largely mirror that of the particle sizes shown in **Figure 4.2**, with the exceptions of sample S10 and S12. We speculate that this trend may reflect formulation-dependent differences that influence both particle size and effective optical properties in a similar manner. A more detailed discussion of this can be found in **Manuscript II**.

The analysis did not, however, reveal any clear indications of heterogeneity within the individual samples. This may indicate that the formulations are relatively homogeneous, or alternatively that any underlying heterogeneity does not contribute to the effective refractive index to be resolved by NSM under the present measurement conditions. This exploratory study of LNP characterization using the NSM platform has therefore identified several directions for future research and method development, which will be outlined in the next and final chapter.

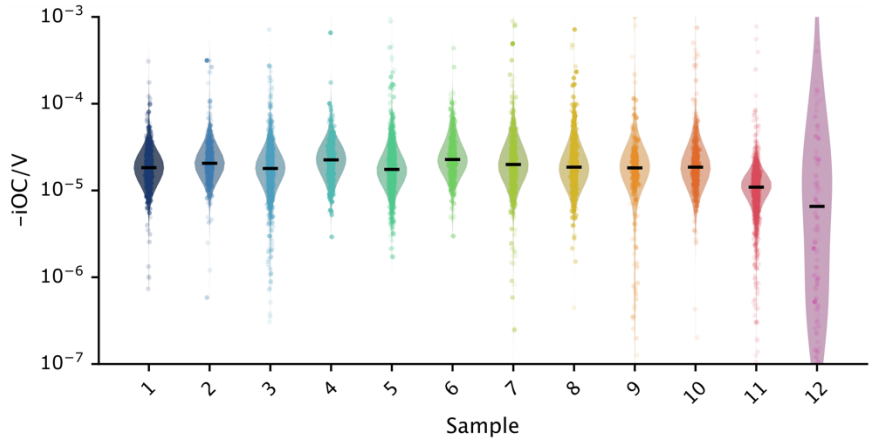

Figure 4.4 Violin plots of *-iOC/V*. *Violin plots of -iOC/V for all twelve LNP samples with individual particle values overlaid. Transparency of point is representative of single-particle trajectory length. The distribution median is depicted by the black line for each sample. The x-axis is in* $\log_{10}$.

5 Conclusions and Outlook

Historically, microscopy has transformed biology by rendering previously invisible systems visible. Today, the challenge lies no longer in simply visualizing biological matter, but to also resolve the complexity and heterogeneity that exists within nanoscale systems. Label-free single particle methods, such as NSM explored in this thesis, offer a potential route towards this by enabling the characterization of biological nanoparticles without perturbation from external labels, or any prior knowledge of the population constituents.

The work presented in this thesis is an early step in this broader direction for the development of NSM into a platform for label-free characterization of heterogeneous biological nanoparticles. In particular, a procedure for the prevention of nonspecific adsorption of particles was presented, together with an exploratory study on lipid nanoparticle characterization. Although the current work does not yet demonstrate resolution of nanoparticle intra-sample heterogeneity, it has established important methodological foundations for future studies of extracellular vesicles, lipid nanoparticles and related biological nanoparticle systems.

In **Chapter 2**, the theoretical and methodological experimental framework underpinning the experiments presented in this thesis was described. This included a description of the nanofluidic devices used, the optical and microscope platform as well as the postprocessing and interpretation of the particle optical signature.

For future studies it will be important to more fully characterize and understand the nanochannel filtration of nanoparticles described in **Section 2.1** and observed for polystyrene samples in **Manuscript II**. To address this, new nanofluidic devices have been designed with a broader range of nanochannel dimensions and smaller incremental size steps, ranging from 370 x 385 nm^2 down to 100 x 85 nm^2. By using samples with well-defined polydispersity in terms of particle size distributions and relative concentrations, the influence of nanochannel filtration on measured particle size distributions can be systematically investigated across different geometries. From a device-design perspective, it may also be possible to reduce the size-dependent filtration by more sophisticated nanochannel inlet geometries. In particular, funnel-shaped channel inlets could potentially facilitate particle entry by reducing steric barriers at the nanochannel-microchannel interface.

Furthermore, as remarked upon in **Section 2.1,** accurate knowledge of the nanochannel dimensions is essential for quantitative interpretation of NSM measurements. The nanochannel cross-sectional area directly influences the translation of diffusivity into particle size and the *iOC* into molecular weight. At present, nanochannel dimensions are determined by destructive characterization through cross-sectional SEM imaging of cleaved devices, followed by manual fitting of the channel geometry. However, this is both labor-intensive and associated with several sources of uncertainty, including limited SEM resolution and ambiguity in defining the precise nanochannel boundaries. In addition, this approach prevents further use of the device and thus has to be done at the conclusion of the study, at which point the data will have to be reanalyzed. An alternative strategy will therefore greatly benefit the workflow from measurement to interpretation. Such a strategy could

involve indirect determination of nanochannel dimensions using calibration samples with known particle size distributions, as it may be possible to estimate the effective nanochannel dimension through back-calculation of the expected particle distributions.

In **Section 2.2.3** the optical platform was described together with its recent extension by a fluorescence imaging arm, currently equipped with a 488 nm excitation laser. In **Manuscript I** it was used for the fluorescence-based imaging of nonspecific adsorption of avidin-FITC. However, the long-term potential of the system lies in synchronized fluorescence and NSM measurements, which are currently under development. Although NSM is fundamentally a label-free technique, correlative fluorescence measurements may provide an important complementary tool during the interpretation and validation of scattering signals, particularly in complex biological samples which contain multiple particle populations in addition to the vesicles of interest. Combining the two techniques may therefore provide an intermediate step toward fully label-free characterization. Furthermore, an integrated fluorescence-NSM platform may enable comparative studies of labeled and unlabeled systems, thereby allowing the influence of fluorescent labeling on particle behavior and properties to be investigated.

The complications of translating *iOC* into molecular weight for complex biological nanoparticles were discussed in **Section 2.3.2**. Unlike proteins, these systems possess heterogeneous and poorly defined compositions consisting of multiple biomolecular constituents with differing optical properties at unknown relative fractions. Furthermore, the larger particle dimensions and nanochannel sizes required for their characterization place the system outside the small-particle regime assumed for protein

measurements, such that higher order multipole contributions become increasingly important to the scattering response. Nevertheless, it may still be possible to infer a value for effective refractive index through calibration against samples with well-defined optical properties. As a proof-of concept, the effective refractive index of liposomes was estimated through calibration using polystyrene samples. This approach will be the primary direction for continued methodological development. Future work will therefore involve more comprehensive modeling of nanoparticle scattering signatures where Mie theory for homogeneous spherical particles will be used to account for deviations from the Rayleigh scattering regime. Extensions based on coated-sphere models may further enable the separation of the optical contributions from the particle interior and the surrounding lipid membrane, yielding more detailed interpretations of the optical signatures.

In **Chapter 3** the origins of nonspecific adsorption at solid-liquid interfaces were described together with geometrical arguments for why such interactions become particularly critical in nanofluidic systems. Addressing this issue was therefore a necessary prerequisite for extending NSM toward characterization of biological nanoparticles, since systems such as lipid nanoparticles and extracellular vesicles have a strong tendency to interact with the silica surfaces of the nanofluidic devices. Such interactions fundamentally compromise reliable characterization, as NSM measurements rely on freely diffusing particle within the nanochannels.

A solution to this problem was presented in **Section 3.4** and **Manuscript I** through surface passivation of the nanochannels based on physisorption of the polymer PLL-g-PEG. Nanochannels with dimensions down to 50 x 50 nm^2 could be successfully coated, and the passivation layer was shown to

substantially reduce nonspecific adsorption through fluorescence imaging of adsorbed avidin-FITC, as well as through NSM measurements of proteins and liposomes. This resulted in significantly improved accuracy of particle size determination. Beyond enabling characterization of lipid-based nanoparticles, the passivation protocol may also broaden the applicability of NSM towards proteins with stronger surface interactions, which were previously difficult to measure. Future work will involve more comprehensive characterization of the passivation layer, including determination of its thickness, uniformity and potential dependence on nanochannel geometry. Furthermore, although outside the scope of the present work, functionalized PLL-g-PEG variants containing specific binding motifs may in the future enable studied of targeted molecular interactions within the NSM platform.

In **Chapter 4** and **Manuscript II**, an exploratory study of lipid nanoparticles using the current implementation of the NSM method was presented. The accuracy and precision of NSM-based particle sizing were evaluated using twelve industrially formulated lipid nanoparticle samples and benchmarked against dynamic light scattering (DLS), nanoparticle tracking analysis (NTA) and cryo- transmission electron microscopy (cryo-TEM), demonstrating overall good agreement across the samples. Furthermore, incorporation of *iOC* as a second dimension enabled additional assessment of the optical properties of the particles. Within the investigated samples, this analysis indicated relatively limited sample heterogeneity. However, given the industrial formulation and optimization of these lipid nanoparticle systems, this might be expected. It therefore remains unclear to what extent the observed homogeneity reflects the true sample populations, and to what extent it may instead arise from limitations in the current NSM methodology.

Future studies should therefore focus on more controlled nanoparticle model systems, for example, nanoparticles formulated with identical compositions but different with respect to cargo loading, measured both individually and in mixed populations. This will further provide an excellent platform for the development of a methodology that translates particle optical signatures into effective refractive indices.

As outlined in this chapter, there are still many challenges that remain before NSM can be established as a platform for reliable characterization of heterogeneous biological nanoparticle systems, and the work presented in this thesis has established several methodological foundations for its continued development. Together, these future investigations point toward a broad range of possibilities for extending NSM toward increasingly complex biological systems.

Exciting times are ahead!

Acknowledgments

It is truly a joy to work on a project such as this, where biology meets physics, meets optics, meets nanotechnology, meets surface chemistry, meets…

I cannot do it on my own, and as such there is a list of people I wish to thank:

First, my supervisor Christoph Langhammer, for giving me the opportunity to work on this project and the freedom to explore. Your encouragement and advice are of momentous help in keeping things moving forward!
Bohdan Yeroshenko, thank you for always taking the time to help me out with whatever query I might have, and for your encouragement at every step. Without you, I might still be stuck trying to align the microscope!
My co-supervisor Joachim Fritzsche, whose expertise in nanofabrication keeps this project going, thank you for all your help and good ideas!
My examiner Henrik Grönbeck, thank you for your feedback on this thesis and your encouragement!
The Langhammer group members and the rest of my colleagues at Chemical Physics, thank you all for your kindness and support, and for making floor 5 a great place to go to every day!
All my co-authors and project members, thank you all for your time, input, sample preparation and knowledge!
Knut and Alice Wallenberg Stiftelse, for funding this project.

Finally, mamma, pappa, bror, Andreas, and all of my friends; thank you for your love and support. I am so excited to spend more time with all of you!

References

1. Wollman, A. J. M., Nudd, R., Hedlund, E. G. & Leake, M. C. From Animaculum to single molecules: 300 years of the light microscope. *Open Biol.* **5**, 150019 (2015).
2. Hooke, R. *Micrographia: Or Some Physiological Descriptions of Minute Bodies Made by Magnifying Glasses, with Observations and Inquiries Thereupon*. (Courier Corporation, 1665).
3. Coons, A. H., Creech, H. J. & Jones, R. Norman. Immunological properties of an antibody containing a fluorescent group. *Proc. Soc. Exp. Biol. Med.* **47**, 200–202 (1941).
4. Chalfie, M., Tu, Y., Euskirchen, G., Ward, W. W. & Prasher, D. C. Green fluorescent protein as a marker for gene expression. *Science (1979).* **263**, 802–805 (1994).
5. Saxton, M. J. & Jacobson, K. Single-particle tracking: applications to membrane dynamics. *Annu. Rev. Biophys.* **26**, 373–399 (1997).
6. Kubitscheck, U. Fluorescence microscopy: single particle tracking. in *Encyclopedic Reference of Genomics and Proteomics in Molecular Medicine* 579–583 (Springer, Berlin, Heidelberg, 2006).
7. Rust, M. J., Bates, M. & Zhuang, X. Sub-diffraction-limit imaging by stochastic optical reconstruction microscopy (STORM). *Nat. Methods* **3**, 793–796 (2006).
8. Hell, S. W. & Wichmann, J. Breaking the diffraction resolution limit by stimulated emission: stimulated-emission-depletion fluorescence microscopy. *Opt. Lett.* **19**, 780–782 (1994).
9. Weisgerber, A. W. & Knowles, M. K. Membrane dynamics are slowed for Alexa594-labeled membrane proteins due to substrate interactions. *BBA Advances* **1**, 100026 (2021).

10. Riback, J. A. *et al.* Commonly used FRET fluorophores promote collapse of an otherwise disordered protein. *Proc. Natl Acad. Sci. USA* **116**, 8889–8894 (2019).
11. Sun, Y. S. *et al.* Effect of fluorescently labeling protein probes on kinetics of protein−ligand reactions. *Langmuir* **24**, 13399–13405 (2008).
12. Swulius, M. T. & Jensen, G. J. The helical MreB cytoskeleton in Escherichia coli MC1000/pLE7 is an artifact of the N-terminal yellow fluorescent protein tag. *J. Bacteriol.* **194**, 6382–6386 (2012).
13. Lakowicz, J. R. *Principles of Fluorescence Spectroscopy*. 3rd edn (Springer, 2006).
14. Ghosh, B. & Agarwal, K. Viewing life without labels under optical microscopes. *Commun. Biol.* **6**, 559 (2023).
15. Taylor, R. W. & Sandoghdar, V. Interferometric scattering (iSCAT) microscopy and related techniques. in *Label-Free Super-Resolution Microscopy* (ed. Astratov, V.) 25–65 (Springer, 2019).
16. Zernike, F. Phase contrast, a new method for the microscopic observation of transparent objects. *Physica* **9**, 686–698 (1942).
17. Ortega Arroyo, J. *et al.* Label-free, all-optical detection, imaging, and tracking of a single protein. *Nano Lett.* **14**, 2065–2070 (2014).
18. Lindfors, K., Kalkbrenner, T., Stoller, P. & Sandoghdar, V. Detection and spectroscopy of gold nanoparticles using supercontinuum white light confocal microscopy. *Phys. Rev. Lett.* **93**, 37401 (2004).
19. Moberg, H. K. *et al.* Label-free mass and size characterization of few-kDa biomolecules by hierarchical vision transformer augmented nanofluidic scattering microscopy. *Nat. Commun.* **17**, 2533 (2026).

20. Špačková, B. *et al.* Label-free nanofluidic scattering microscopy of size and mass of single diffusing molecules and nanoparticles. *Nat. Methods* **19**, 751–758 (2022).
21. Xu, S., Hu, Z., Song, F., Xu, Y. & Han, X. Lipid nanoparticles: composition, formulation, and application. *Mol. Ther. Methods Clin. Dev.* **33**, 101463 (2025).
22. Carney, R. P. *et al.* Harnessing extracellular vesicle heterogeneity for diagnostic and therapeutic applications. *Nat. Nanotechnol.* **20**, 14–25 (2025).
23. Kumar, M. A. *et al.* Extracellular vesicles as tools and targets in therapy for diseases. *Signal Transduct. Target. Ther.* **9**, 27 (2024).
24. Hou, X., Zaks, T., Langer, R. & Dong, Y. Lipid nanoparticles for mRNA delivery. *Nat. Rev. Mater.* **6**, 1078–1094 (2021).
25. Swetha, K. *et al.* Recent advances in the lipid nanoparticle-mediated delivery of mRNA vaccines. *Vaccines (Basel).* **11**, 658 (2023).
26. Jacob, E. M., Huang, J. & Chen, M. Lipid nanoparticle-based mRNA vaccines: a new frontier in precision oncology. *Precis. Clin. Med.* **7**, pbae017 (2024).
27. Chen, X. *et al.* Structural characterization of mRNA lipid nanoparticles (LNPs) in the presence of mRNA-free LNPs. *J. Control. Release* **386**, 114082 (2025).
28. Li, S. *et al.* Payload distribution and capacity of mRNA lipid nanoparticles. *Nat. Commun.* **13**, 5561 (2022).
29. Padilla, M. S. *et al.* Elucidating lipid nanoparticle properties and structure through biophysical analyses. *Nat. Biotechnol.* (2025)
30. Sych, T. *et al.* High-throughput measurement of the content and properties of nano-sized bioparticles with single-particle profiler. *Nat. Biotechnol.* **42**, 587–590 (2024).

31. Li, X. *et al.* Extracellular vesicle-based point-of-care testing for diagnosis and monitoring of Alzheimer's disease. *Microsyst. Nanoeng.* **11**, 65 (2025).
32. Kim, B. *et al.* Size control of lipid nanoparticles via simulation-based design of a microfluidic chip and its effect on mRNA delivery in vitro and in vivo. *J. Nanobiotechnology* **23**, 797 (2025).
33. Mashima, R. & Takada, S. Lipid nanoparticles: a novel gene delivery technique for clinical application. *Curr. Issues Mol. Biol.* **44**, 5013–5027 (2022).
34. Nogueira, S. S. *et al.* Analytical techniques for the characterization of nanoparticles for mRNA delivery. *Eur. J. Pharm. Biopharm* **198**, 114235 (2024).
35. Kashkanova, A. D., Blessing, M., Gemeinhardt, A., Soulat, D. & Sandoghdar, V. Precision size and refractive index analysis of weakly scattering nanoparticles in polydispersions. *Nat. Methods* **19**, 586–593 (2022).
36. Penders, J. *et al.* Single particle automated Raman trapping analysis. *Nat. Commun.* **9**, 4256 (2018).
37. Hong, I. *et al.* Rapid trapping and label-free optical characterization of single nanoscale extracellular vesicles and nanoparticles in solution. *Light Sci. Appl.* **15**, 180 (2026).
38. Wang, R. & Lin, S. Pore model for nanofiltration: history, theoretical framework, key predictions, limitations, and prospects. *J. Memb. Sci.* **620**, 118809 (2021).
39. Dechadilok, P. & Deen, W. M. Hindrance factors for diffusion and convection in pores. *Ind. Eng. Chem. Res.* **45**, 6953–6959 (2006).
40. Bohren, C. F. & Huffman, D. R. *Absorption and Scattering of Light by Small Particles*. (Wiley, 1983).

41. Taylor, R. W. & Sandoghdar, V. Interferometric scattering microscopy: seeing single nanoparticles and molecules via Rayleigh scattering. *Nano Lett.* **19**, 4827–4835 (2019).
42. Zhang, P. *et al.* Plasmonic scattering imaging of single proteins and binding kinetics. *Nat. Methods* **17**, 1010–1017 (2020).
43. Ruzin, S. E. *Techniques in Light Microscopy*. (Oxford University Press, 2024).
44. Vestergaard, C. L., Blainey, P. C. & Flyvbjerg, H. Optimal estimation of diffusion coefficients from single-particle trajectories. *Phys. Rev. E* **89**, 22726 (2014).
45. Maguire, C. M., Rösslein, M., Wick, P. & Prina-Mello, A. Characterisation of particles in solution – a perspective on light scattering and comparative technologies. *Sci. Technol. Adv. Mater.* **19**, 732–745 (2018).
46. McMeekin, T. L., Wilensky, M. & Groves, M. L. Refractive indices of proteins in relation to amino acid composition and specific volume. *Biochem. Biophys. Res. Commun.* **7**, 151–156 (1962).
47. McMeekin, T. L., Groves, M. L. & Hipp, N. J. Refractive indices of amino acids, proteins, and related substances. in *Amino Acids and Serum Proteins* vol. 44 54–66 (American Chemical Society, 1964).
48. Young, G. *et al.* Quantitative mass imaging of single biological macromolecules. *Science.* **360**, 423–427 (2018).
49. Khago, D., Bierma, J. C., Roskamp, K. W., Kozlyuk, N. & Martin, R. W. Protein refractive index increment is determined by conformation as well as composition. *J. Phys. Condens. Matter* **30**, 435101 (2018).
50. Wiscombe, W. J. Improved Mie scattering algorithms. *Appl. Opt.* **19**, 1505–1509 (1980).

51. Sihvola, A. *Electromagnetic Mixing Formulas and Applications*. (The Institution of Engineering and Technology, 1999).
52. García Rodríguez, B. *et al.* Optical label-free microscopy characterization of dielectric nanoparticles. *Nanoscale* **17**, 8336–8362 (2025).
53. Lichtenberg, J. Y., Ling, Y. & Kim, S. Non-specific adsorption reduction methods in biosensing. *Sensors* **19**, 2488 (2019).
54. Rabe, M., Verdes, D. & Seeger, S. Understanding protein adsorption phenomena at solid surfaces. *Adv. Colloid Interface Sci.* **162**, 87–106 (2011).
55. Norde, W. My voyage of discovery to proteins in flatland …and beyond. *Colloids Surf. B Biointerfaces* **61**, 1–9 (2008).
56. Hlady, V. & Buijs, J. Protein adsorption on solid surfaces. *Curr. Opin. Biotechnol.* **7**, 72–77 (1996).
57. Norde, W. Driving forces for protein adsorption at solid surfaces. *Macromol. Symp.* **103**, 5–18 (1996).
58. Stutz, H. Protein attachment onto silica surfaces – a survey of molecular fundamentals, resulting effects and novel preventive strategies in CE. *Electrophoresis* **30**, 2032–2061 (2009).
59. Kubiak-Ossowska, K., Jachimska, B., Al Qaraghuli, M. & Mulheran, P. A. Protein interactions with negatively charged inorganic surfaces. *Curr. Opin. Colloid Interface Sci.* **41**, 104–117 (2019).
60. Roach, P., Farrar, D. & Perry, C. C. Interpretation of protein adsorption: surface-induced conformational changes. *J. Am. Chem. Soc.* **127**, 8168–8173 (2005).
61. Martin, L., Bilek, M. M., Weiss, A. S. & Kuyucak, S. Force fields for simulating the interaction of surfaces with biological molecules. *Interface Focus* **6**, 20150045 (2016).

62. Norde, W. Adsorption of proteins at solid-liquid interfaces. *Cells Mater.* **5**, 97–112 (1995).
63. Cremer, P. S. & Boxer, S. G. Formation and spreading of lipid bilayers on planar glass supports. *J. Phys. Chem. B* **103**, 2554–2559 (1999).
64. Liu, P., Chen, G. & Zhang, J. A review of liposomes as a drug delivery system: current status of approved products, regulatory environments, and future perspectives. *Molecules* **27**, 1372 (2022).
65. Elsharkasy, O. M. *et al.* Extracellular vesicles as drug delivery systems: why and how? *Adv. Drug Deliv. Rev.* **159**, 332–343 (2020).
66. Richter, R. P., Bérat, R. & Brisson, A. R. Formation of solid-supported lipid bilayers: an integrated view. *Langmuir* **22**, 3497–3505 (2006).
67. Keller, C. A. & Kasemo, B. Surface specific kinetics of lipid vesicle adsorption measured with a quartz crystal microbalance. *Biophys. J.* **75**, 1397–1402 (1998).
68. Dimitrievski, K. & Kasemo, B. Influence of lipid vesicle composition and surface charge density on vesicle adsorption events: a kinetic phase diagram. *Langmuir* **25**, 8865–8869 (2009).
69. Reimhult, E., Höök, F. & Kasemo, B. Intact vesicle adsorption and supported biomembrane formation from vesicles in solution: influence of surface chemistry, vesicle size, temperature, and osmotic pressure. *Langmuir* **19**, 1681–1691 (2003).
70. Tero, R. Substrate effects on the formation process, structure and physicochemical properties of supported lipid bilayer. *Materials (Basel)* **5**, 2658–2680 (2012).

71. Hallal, S., Tűzesi, Á., Grau, G. E., Buckland, M. E. & Alexander, K. L. Understanding the extracellular vesicle surface for clinical molecular biology. *J. Extracell. Vesicles* **11**, e12260 (2022).

72. Schürz, M. *et al.* EVAnalyzer: high content imaging for rigorous characterisation of single extracellular vesicles using standard laboratory equipment and a new open-source ImageJ/Fiji plugin. *J. Extracell. Vesicles* **11**, 12282 (2022).

73. Pachane, B. C., Carlson, B., Queen, S. E., Selistre-de-Araujo, H. S. & Witwer, K. W. Exploring the adhesion properties of extracellular vesicles for functional assays. *J. Extracell. Biol* **4**, e70042 (2025).

74. Federici, S. *et al.* Interaction of extracellular vesicles with Si surface studied by nanomechanical microcantilever sensors. *Appl. Sci* **8**, 404 (2018).

75. Grad, P., Edwards, K. & Agmo Hernández, V. Adhesion and structural changes of PEGylated lipid nanocarriers on silica surfaces. *Physchem* **1**, 133–151 (2021).

76. Whitesides, G. M. The origins and the future of microfluidics. *Nature* **442**, 368–373 (2006).

77. Schoch, R. B., Han, J. & Renaud, P. Transport phenomena in nanofluidics. *Rev. Mod. Phys.* **80**, 839–883 (2008).

78. Persson, F. *et al.* Lipid-based passivation in nanofluidics. *Nano Lett.* **12**, 2260–2265 (2012).

79. van Hijkoop, V. J., Dammers, A. J., Malek, K. & Coppens, M.-O. Water diffusion through a membrane protein channel: a first passage time approach. *J. Chem. Phys.* **127**, 085101 (2007).

80. Redner, S. A first look at first-passage processes. *Physica A* **631**, 128545 (2023).

81. Durand, N. F. Y. *et al.* Direct observation of transitions between surface-dominated and bulk diffusion regimes in nanochannels. *Anal. Chem.* **81**, 5407–5412 (2009).

82. Chen, S., Li, L., Zhao, C. & Zheng, J. Surface hydration: principles and applications toward low-fouling/nonfouling biomaterials. *Polymer (Guildf).* **51**, 5283–5293 (2010).

83. Ostuni, E., Chapman, R. G., Holmlin, R. E., Takayama, S. & Whitesides, G. M. A survey of structure−property relationships of surfaces that resist the adsorption of protein. *Langmuir* **17**, 5605–5620 (2001).

84. Israelachvili, J. N. & Pashley, R. M. Molecular layering of water at surfaces and origin of repulsive hydration forces. *Nature* **306**, 249–250 (1983).

85. Leng, C., Sun, S., Zhang, K., Jiang, S. & Chen, Z. Molecular level studies on interfacial hydration of zwitterionic and other antifouling polymers in situ. *Acta Biomater.* **40**, 6–15 (2016).

86. Nagasawa, D., Azuma, T., Noguchi, H., Uosaki, K. & Takai, M. Role of interfacial water in protein adsorption onto polymer brushes as studied by SFG spectroscopy and QCM. *J. phys. Chem. C* **119**, 17193–17201 (2015).

87. Alexander, S. Adsorption of chain molecules with a polar head a scaling description. *J. Phys* **38**, 983–987 (1977).

88. Zhao, B. & Brittain, W. J. Polymer brushes: surface-immobilized macromolecules. *Prog. Polym. Sci.* **25**, 677–710 (2000).

89. Zheng, J., Li, L., Chen, S. & Jiang, S. Molecular simulation study of water interactions with oligo (ethylene glycol)-terminated alkanethiol self-assembled monolayers. *Langmuir* **20**, 8931–8938 (2004).

90. Li, L., Chen, S., Zheng, J., Ratner, B. D. & Jiang, S. Protein adsorption on oligo(ethylene glycol)-terminated alkanethiolate self-assembled monolayers: the molecular basis for nonfouling behavior. *J. Phys. Chem. B* **109**, 2934–2941 (2005).

91. Bernards, M. T., Cheng, G., Zhang, Z., Chen, S. & Jiang, S. Nonfouling polymer brushes via surface-initiated, two-component atom transfer radical polymerization. *Macromolecules* **41**, 4216–4219 (2008).

92. Verma, C. *et al.* Zwitterions and betaines as highly soluble materials for sustainable corrosion protection: Interfacial chemistry and bonding with metal surfaces. *Adv. Colloid Interface Sci.* **324**, 103091 (2024).

93. Zhang, Y. *et al.* Fundamentals and applications of zwitterionic antifouling polymers. *J. Phys. D Appl. Phys.* **52**, 403001 (2019).

94. Castellana, E. T. & Cremer, P. S. Solid supported lipid bilayers: from biophysical studies to sensor design. *Surf. Sci. Rep.* **61**, 429–444 (2006).

95. He, M. *et al.* Zwitterionic materials for antifouling membrane surface construction. *Acta Biomater.* **40**, 142–152 (2016).

96. van Meer, G., Voelker, D. R. & Feigenson, G. W. Membrane lipids: where they are and how they behave. *Nat. Rev. Mol. Cell Biol.* **9**, 112–124 (2008).

97. Glasmästar, K., Larsson, C., Höök, F. & Kasemo, B. Protein adsorption on supported phospholipid bilayers. *J. Colloid Interface Sci.* **246**, 40–47 (2002).

98. Sut, T. N., Yoon, B. K., Jeon, W.-Y., Jackman, J. A. & Cho, N.-J. Supported lipid bilayer coatings: fabrication, bioconjugation, and diagnostic applications. *Appl. Mater. Today* **25**, 101183 (2021).

99. Prime, K. L. & Whitesides, G. M. Self-assembled organic monolayers: model systems for studying adsorption of proteins at aurfaces. *Science.* **252**, 1164–1167 (1991).

100. Jeon, S. I., Lee, J. H., Andrade, J. D. & De Gennes, P. G. Protein—surface interactions in the presence of polyethylene oxide: I. Simplified theory. *J. Colloid Interface Sci.* **142**, 149–158 (1991).

101. Gautrot, J. E. *et al.* Exploiting the superior protein resistance of polymer brushes to control single cell adhesion and polarisation at the micron scale. *Biomaterials* **31**, 5030–5041 (2010).

102. Lee, B. S. *et al.* Surface-initiated, atom transfer radical polymerization of oligo(ethylene glycol) methyl ether methacrylate and subsequent click chemistry for bioconjugation. *Biomacromolecules* **8**, 744–749 (2007).

103. Gidi, Y., Bayram, S., Ablenas, C. J., Blum, A. S. & Cosa, G. Efficient one-step PEG-silane passivation of glass surfaces for single-molecule fluorescence studies. *ACS Appl. Mater. Interfaces* **10**, 39505–39511 (2018).

104. Sofia, S. J., Premnath, V. & Merrill, E. W. Poly(ethylene oxide) grafted to silicon surfaces: grafting density and protein adsorption. *Macromolecules* **31**, 5059–5070 (1998).

105. Emilsson, G. *et al.* Strongly stretched protein resistant poly(ethylene glycol) brushes prepared by grafting-to. *ACS Appl. Mater. Interfaces* **7**, 7505–7515 (2015).

106. Andersson, J. *et al.* Polymer brushes on silica nanostructures prepared by aminopropylsilatrane click chemistry: superior antifouling and biofunctionality. *ACS Appl. Mater. Interfaces* **15**, 10228–10239 (2023).

107. Kenausis, G. L. *et al.* Poly(l-lysine)-g-poly(ethylene glycol) layers on metal oxide surfaces: attachment mechanism and effects of polymer architecture on resistance to protein adsorption. *J. Phys. Chem. B* **104**, 3298–3309 (2000).

108. Huang, N.-P. *et al.* Poly(l-lysine)-g-poly(ethylene glycol) layers on metal oxide surfaces: surface-analytical characterization and resistance to serum and fibrinogen adsorption. *Langmuir* **17**, 489–498 (2001).

109. Pasche, S., De Paul, S. M., Vörös, J., Spencer, N. D. & Textor, M. Poly(l-lysine)-graft-poly(ethylene glycol) assembled monolayers on niobium oxide surfaces: a quantitative study of the influence of polymer interfacial architecture on resistance to protein adsorption by ToF-SIMS and in situ OWLS. *Langmuir* **19**, 9216–9225 (2003).

110. Heuberger, M., Drobek, T. & Spencer, N. D. Interaction forces and morphology of a protein-resistant poly(ethylene glycol) layer. *Biophys. J.* **88**, 495–504 (2005).

111. Tosatti, S. *et al.* Peptide functionalized poly(l-lysine)-g-poly(ethylene glycol) on titanium: resistance to protein adsorption in full heparinized human blood plasma. *Biomaterials* **24**, 4949–4958 (2003).

112. Salehirozveh, M., Kure Larsen, A.-K., Stojmenovic, M., Thei, F. & Dong, M. In-situ PLL-g-PEG functionalized nanopore for enhancing protein characterization. *Chem. Asian J.* **18**, e202300515 (2023).

113. Marie, R., Beech, J. P., Vörös, J., Tegenfeldt, J. O. & Höök, F. Use of PLL-g-PEG in micro-fluidic devices for localizing selective and specific protein binding. *Langmuir* **22**, 10103–10108 (2006).

114. Schoch, R. B., Cheow, L. F. & Han, J. Electrical detection of fast reaction kinetics in nanochannels with an induced flow. *Nano Lett.* **7**, 3895–3900 (2007).

115. Schoch, R. L. & Lim, R. Y. H. Non-interacting molecules as innate structural probes in surface plasmon resonance. *Langmuir* **29**, 4068–4076 (2013).

116. Huang, N.-P., Vörös, J., De Paul, S. M., Textor, M. & Spencer, N. D. Biotin-derivatized poly(l-lysine)-g-poly(ethylene glycol): a novel polymeric interface for bioaffinity sensing. *Langmuir* **18**, 220–230 (2002).

117. Zhen, G. *et al.* Nitrilotriacetic acid functionalized graft copolymers: a polymeric interface for selective and reversible binding of histidine-tagged proteins. *Adv. Funct. Mater.* **16**, 243–251 (2006).

118. Qin, S. *et al.* mRNA-based therapeutics: powerful and versatile tools to combat diseases. *Signal Transduct. Target. Ther.* **7**, 166 (2022).

119. Ma, Y., VanKeulen-Miller, R. & Fenton, O. S. mRNA lipid nanoparticle formulation, characterization and evaluation. *Nat. Protoc.* **20**, 2618–2651 (2025).

120. Schober, G. B., Story, S. & Arya, D. P. A careful look at lipid nanoparticle characterization: analysis of benchmark formulations for encapsulation of RNA cargo size gradient. *Sci. Rep.* **14**, 2403 (2024).

121. Udepurkar, A. *et al.* Structure and morphology of lipid nanoparticles for nucleic acid drug delivery: a review. *ACS Nano* **19**, 21206–21242 (2025).

122. Brader, M. L. *et al.* Encapsulation state of messenger RNA inside lipid nanoparticles. *Biophys. J.* **120**, 2766–2770 (2021).

123. Li, X. *et al.* Design strategies for novel lipid nanoparticle for mRNA vaccine and therapeutics: current understandings and future perspectives. *MedComm (Beijing).* **6**, e70414 (2025).
124. Babick, F. Chapter 3.2.1 - Dynamic light scattering (DLS). in *Characterization of Nanoparticles* (eds. Hodoroaba, V.-D., Unger, W. E. S. & Shard, A. G.) 137–172 (Elsevier, 2020).
125. Filipe, V., Hawe, A. & Jiskoot, W. Critical evaluation of nanoparticle tracking analysis (NTA) by NanoSight for the measurement of nanoparticles and protein aggregates. *Pharm. Res.* **27**, 796–810 (2010).
126. Hole, P. Chapter 3.1.2 - Particle Tracking Analysis (PTA). in *Characterization of Nanoparticles* (eds. Hodoroaba, V.-D., Unger, W. E. S. & Shard, A. G.) 79–96 (Elsevier, 2020).
127. Mittal, V. & Matsko, N. B. Visualization of organic–inorganic nanostructures in liquid. in *Analytical Imaging Techniques for Soft Matter Characterization* 13–29 (Springer, Berlin, Heidelberg, 2012).
128. Peretz Damari, S. *et al.* Practical aspects in size and morphology characterization of drug-loaded nano-liposomes. *Int. J. Pharm.* **547**, 648–655 (2018).